Title
Three approaches to economical photovoltaics: conformal Cu2S, organic luminescent films, and PbSe nanocrystal superlattices

Permalink
https://escholarship.org/uc/item/7c03d8fd

Author
Carbone, Ian Anthony

Publication Date
2013

Peer reviewed|Thesis/dissertation

UNIVERSITY OF CALIFORNIA

SANTA CRUZ

THREE APPROACHES TO ECONOMICAL PHOTOVOLTAICS: CONFORMAL Cu$_2$S, ORGANIC LUMINESCENT FILMS, AND PbSe NANOCRYSTAL SUPERLATTICES

A dissertation submitted in partial satisfaction of the requirements for the degree of

DOCTOR OF PHILOSOPHY

in

PHYSICS

by

Ian A. Carbone

June 2013

The Dissertation of Ian A. Carbone
is approved:

———————————————
Professor Sue Carter, Chair

———————————————
Professor Glenn Alers

———————————————
Professor Gergely Zimanyi

———————————————
Tyrus Miller
Vice Provost and Dean of Graduate Studies

Table of Contents

List of Figures

List of Tables

Abstract

Three approaches to economical photovoltaics: conformal Cu_2S, organic

luminescent films, and PbSe nanocrystal superlattices

by

Ian A. Carbone

Three routes to more efficient photovoltaics using conformal Cu_2S, organic luminescent films, and nanocrystalline PbSe films are outlined below. Properties of these materials are investigated experimentally and numerically in separate studies.

In the first study, chemical vapor deposition (CVD) processes were used to fabricate Cu_2S using hydrogen sulfide and the metal-organic precursor, KI5. The alternating exposure of mesoporous TiO_2 and planar ZnO to the two precursors resulted in films that penetrated porous structures and deposited at a constant rate of 0.08nm/cycle over the temperature range 150°C-400°C. Sheet resistance and optical absorption measurements suggest the presence of a metallic copper-poor phase of less than 100nm thick forming at the Cu_2S/substrate boundary.

In a separate study, organic films doped with luminescent dyes were placed above CdTe/CdS solar cells to convert high energy photons to lower energies, better matched to the CdTe/CdS quantum efficiency peak. Efficiency improvements of up to 8.5% were obtained after optimizing dye concentration, dye chemistry, and the host material. Long-term stability tests show that the organic films are stable for at least

5000 hours under 1 sun illumination provided that the dye is encapsulated in an oxygen and water free environment.

Finally, a Monte Carlo model was developed to simulate electron and hole transport in nanocrystalline PbSe films. Transport is carried out as a series of thermally activated tunneling events between neighboring sites on a cubic lattice. Each site, representing an individual nanocrystal, is assigned a size-dependent electronic structure, and the effects of crystal size, charging, inter-crystal coupling, and energetic disorder on electron and hole mobilities/conductivities are investigated. Results of simulated field effect measurements confirm that electron mobilities and conductivities increase by an order of magnitude when the average nanocrystal diameter is increased in the 3-5nm range. Electron mobilities/conductivities begin to decrease for average nanocrystal diameters above 6nm. Our model suggests that as crystal size increases, fewer hops are required to traverse a given film length and that site energy disorder significantly inhibits transport in films composed of smaller nanocrystals. The dip in transport above 6nm can be explained by a decrease in tunneling amplitudes and by carrier interactions, which become more frequent at larger crystal diameters. Using a nearly identical set of parameter values as the electron simulations, hole simulations confirm experimental mobilities, which increase with nanocrystal size over two orders of magnitude.

To the pursuit of a more sustainable society.

Acknowledgments

I want to thank my friends and family. Without their support and guidance, I would

never have finished this degree.

Thanks to Gergely Zimanyi for providing me with encouragement and direction for the

modeling portion of this dissertation.

Thanks to Glenn Alers for advising me on the LDS film and Cu_2S work.

Special thanks to Sue for her inspiring commitment to her students.

Thanks to all of my lab-mates for all of their help and support.

Part I

Background

Chapter 1

Introduction

1.1 Motivation

1.1.1 Energy

From the discovery of fire to the invention of the atomic bomb, consumable energy has shaped civilization. Energy allows us to move about in vehicles, to develop and practice modern medicine, and to build the infrastructure of our cities. Consumable energy allows us to share information at the speed of light and to feed our population. Figure 1.1 provides a sense of the importance of energy to economic productivity. The most wealthy countries require the most energy to sustain, and as nations develop they generally require more energy. Increasing energy consumption may not always be necessary for improving our quality of life, however, no one can dispute the integral role that energy has had and continues to have in shaping the political landscape and the environment that we live in. Energy security is a primary objective of nearly every

nation.
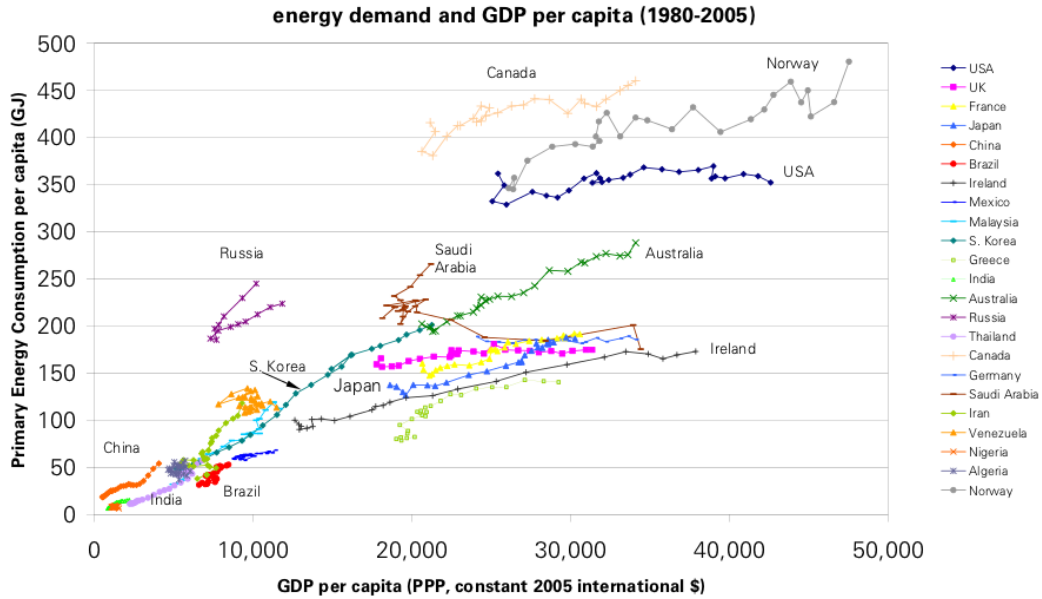
Figure 1.1: Energy demand and GDP per capita for 23 countries from 1980-2005

In 2012, the world population consumed roughly 5.2×10^{11} gigajoules of energy - the equivalent of more than 12 billion tons of oil.[9] The major fossil fuels (oil, coal, and natural gas) account for 80% of this consumption,[9] and we will almost certainly see an increase in total energy and fossil fuel consumption in the near future. In 2012, global energy consumption rose by 1.8%, largely due to increasing demand in developing countries like China and India. BP predicts that by 2030, energy used for power generation will grow by 49%, accounting for 57% of global primary energy growth.[9] CO_2 levels in the atmosphere will likely increase by 28%, and fossil fuels will be responsible 82% of consumable energy.[9] For those who are concerned about the political, social,

3

and environmental consequences of burning fossil fuels, these numbers are daunting.

In this introduction, I will try to highlight the major limitations of the dominant energy production mechanisms in order to motivate the development of solar energy technologies and the research presented in this dissertation.

1.1.2 Social/Economic

There are a number of "hidden costs" associated fossil fuels that may not be immediately obvious when we purchase our energy from the power company or the gas station. The consumer does not pay for these costs directly, but society as whole must compensate for these effects. Hidden health costs in the United States alone are estimated to be about $120 billion per year, largely due to premature deaths caused by fossil fuel-derived air pollution.[92] Approximately 20,000 people die prematurely every year from lung damage caused by soot released by the combustion of fossil fuels.[92]

The Deepwater Horizon explosion (2010), the Sago Mine disaster (2006) , and the Upper Big Branch Mine disaster (2010) represent striking examples of how laborers in the energy sector often suffer worst of these hidden costs. According to the Bureau of Labor Statistics, mining remains the second most dangerous occupation in America,[71] and conditions in the developing world are often significantly worse. Some estimates say as many as 20,000 miners die in accidents each year in Chinese coal mines.[24] The communities that support fuel extraction are also subject to more subtle health effects. Coal mining communities have a "70% increased risk for developing kidney disease, a 64% increased risk for developing chronic obstructive pulmonary diseases (COPD) such

4

as emphysema, and are 30% more likely to report high blood pressure."[34] In a 2009 Journal of American Medical Association article on energy production work environments Steven Sumner, M.D., writes, "if renewable technologies were to, at minimum, eliminate the fossil fuel extraction phase, which is unique to the fossil fuel cycle, current trends suggest that more than 1300 worker deaths could be averted [in the US] in the coming decade."[83]

The most convincing economic argument against fossil fuels might be the reality of their diminishing availability. The International Energy Agency (IEA) reports that the production of conventional crude oil peaked in 2006.[3] Some experts are predicting that peak coal will occur as soon as 2048.[63] As we begin to run out these resources, we are increasingly relying on unconventional fossil fuel sources that are expensive and environmentally costly to harvest. Fuel costs are rising precipitously as fuel resources become more difficult to access, and the market is becoming more volatile as the competition over the remaining resources escalates. Higher and more variable prices mean a less productive economy. Rising oil prices, for-example, have played major role in the past nine global recessions.[82] As conventional energy supplies run out, nations will inevitably shift to renewable technologies. We can ease the economic shock of running out of fossil fuels and increase market stability by developing renewable resources sooner rather than later.

1.1.3 Political

Since the formation of Organization for Petroleum Exporting Countries (OPEC) in 1960, oil importers have engaged in a turbulent tug of war with exporting countries to keep oil prices consistent with economic needs. OPEC has periodically adjusted production rates, "cleansing" and "squeezing" the market, in order to undermine rivals and to maximize profits. Political instabilities and competition within and among oil exporting countries also served to increase market volatility. When prices were particularly high, as they were during the energy crisis of the 70's and 80's, global economies stalled and the result was widespread recession. When prices were too low as they were the late 80's/early 90's, oil refineries and distributors lost billions of dollars in revenues. Both extremes place enormous pressure on oil importers to maintain a healthy economies and high standards of living.

Market volatility is not the only political cost of oil dependency. Iran and Saudi Arabia are two of the world's largest oil exporters. They are also two major threats to political stability in the Middle East. Iran has used oil profits to fund terrorist groups in Lebanon and Palestine. Saudi Arabia has used its wealth to advance radical mosques and the Islamic 'revolution' in places like Afghanistan and Pakistan.[82] S. David Freeman, an energy advisor in the Carter administration writes,

> "Oil money is at the heart of what is financing terrorism as well as Iran's nuclear program. Remember that Osama bin Laden originated from Saudi Arabia, and it is Saudi Arabian oil money that has financed his terrorism... The United States' ability to make peace in the world is badly constrained by our fear of the 'oil weapon' being used by nations such as Saudi Arabia and Iran."[30]

Competition over oil revenues and resources have also led to full-blown military campaigns. The 1980 Iraqi invasion of Iran and the 1989 invasion of Kuwait were both motivated by disputes over oil revenues.[82] Some contend the US military response to the first gulf war and the 2003 invasion of Iraq represented a shift in US policy towards forceful intervention as a means to secure access to Middle Eastern oil.[82] Conflict has also spread beyond the Middle East and created civil unrest in countries like Venezuela and Nigeria.[82]

As rapidly industrializing countries like China and India increase oil demand, and as resources begin to dwindle, the political landscape will become even more strained. In a 2008 survey of America's top security experts, respondents reported that the US government's top priority should be to reduce reliance on foreign oil in order to reduce terror threats.[29] The globalized oil industry is becoming increasingly risky for importers and oil exporters.

1.1.4 Environmental

The Deepwater Horizon disaster, the Exxon-Valdez oil spill, and the 2008 Kingston Fossil Plant coal ash spill are dramatic examples of environmental disasters related to fossil fuels. They are also events that bring awareness to the extraction, distribution, and energy production steps in the fossil fuel economy.

Extraction methods for collecting oil, coal, and gas vary, but in most cases the environmental impacts are similar. According to the EPA, drilling and mining practices release methane, a powerful greenhouse gas into our atmosphere.[4] Large

amounts of water used to pressurize wells or to clean coal are often returned to the environment contaminated with heavy metals and harmful chemicals where they can destroy ecosystems and pollute drinking water.[4] Coal mining is particularly harmful as it can disrupt watersheds, destroy vegetation, and create erosion problems resulting in landslides and flooding.[47]

Hydraulic fracturing is a relatively new process that is used to extract unconventional oil and natural gas resources. It has become the focus of heated public and scientific debate due to concerns around the possible contamination of ground water with carcinogenic compounds and methane.[73, 21, 40] While the severity of the impact of hydraulic fracturing is still under debate, it is worth noting that local governments in South Africa and Canada are suspending the use of the "fracking" technique.[2, 89, 43] France and Vermont have banned the process outright, citing concerns for human and environmental safety.[74, 61]

The combustion fossil fuels (coal in particular) releases harmful particulates, heavy metals, sulfur oxides, nitrogen oxides, mercury, carbon monoxide, and ozone, which are regulated by the Environmental Protection Agency as environmental pollutants.[47] Vehicle emissions produce about 40-50% of nitrogen oxides that the US emits into atmosphere.[47] Coal-fired power plants produce 80% of the sulfur dioxide and 30% of the nitrogen oxides that is emitted, and it is these two ingredients that react with water to create acid rain.[47] When acid rain travels back down to the earth's surface in the form of rain or fog, it is harmful to a variety and plants and aquatic life. It also damages buildings and vehicles and reduces atmospheric visibility.[47]

Greenhouse gases released by fossil fuel combustion, such as methane, nitrogen oxide, ozone, and most importantly, CO_2 are the leading cause of anthropogenic global warming and climate change. More frequent, highly-destructive weather events such as hurricanes, droughts, fires, and floods are likely consequences of climate change.[47] So are the increased spread of tropical diseases, the loss of species due to permanent changes in ecological habitats, and the destruction of low-lying communities and nations as the result of rising sea levels.[47] Experts suggest that as temperatures rise the quantity and quality of freshwater resources will decline,[35] and regions such as central Africa and China that struggle with drought and famine will only continue to loose agricultural productivity.[82] Meanwhile, some of the poorest Asian countries will loose crops because of too much rain.[82]

Approximately 40% of America's CO_2 emissions are produced by coal-fired power plants, while vehicle emissions account for about 33%.[47] Climate change is the greatest long-term challenge that humans face, and for this reason alone, it is essential that we begin moving away from fossil fuels and towards low-impact renewable sources.

1.2 Solar

In one hour, the Sun provides the Earth with enough energy, in the form sunlight, to power our civilization for more than a year.[95] While harvesting the majority of this energy is neither practical nor possible, it is a statistic that conveys the enormous potential of the solar resource.

9

Solar cells are primarily used to convert sunlight into electricity, and are largely considered as a potential replacement for coal and natural gas (which supply roughly 67% of electricity in the United States).[1] However, the growing popularity of electric vehicles means solar could also supply a significant portion of future transportation energy, and significantly reduce oil consumption.

Solar has a number of advantages over fossil fuel energy production. While solar panel manufacturing is energy intensive and can create harmful byproducts, these impacts are generally a one-time cost for a product that produces clean energy for decades. Throughout its functional lifetime, a solar panel will produce no pollution and emit no greenhouse gases. Relatively little material needs to be extracted from the earth for solar cell production, and coal, oil, and natural gas pose significantly greater threats to the environment and to the communities surrounding the resource extraction.[83] While some solar technologies do employ toxic materials, a well constructed solar panel will not leach its contents into the surrounding environment. Nearly all manufacturers will recycle their panels at the end of their lifetimes at not additional cost to the consumer.

Unlike fossil fuel reserves, which might last another hundred years, the solar resource will likely outlast humanity.[1] This provides two major advantages. First of all, a consistent source of energy, which is not subject to market volatility and wild price fluctuations, means more economic stability. Secondly, solar energy provides a path towards energy security and increased national security. Resource-rich countries have less leverage over the global economy when more countries are able to supply their own

energy. By developing solar resources, poor countries could have a pathway towards a higher standard of living, and wealthy countries could avoid dealing with unstable regimes while supporting their own economic growth.

Solar, however, does have drawbacks. Solar energy production requires significant land resources when implemented at the utility scale, and there are serious concerns about the environmental impacts of solar farms on sensitive ecosystems. Another major drawback of solar is that sunshine is intermittent, and unlike fossil fuels, sunlight cannot be stockpiled. Back-up systems and storage facilities must be used in tandem with solar power generation in order to provide a reliable energy supply. In many locations, this is simply not economical for utility power production.

Despite its limitations, many believe that solar provides a better alternative to fossil fuel energy production. To facilitate the large scale adoption of solar and other renewable technologies, two major changes need to happen. First, fossil fuel hidden costs need to be thoroughly considered so that citizens have economic incentive to preserve their environment. Secondly, we must find ways to reduce the costs of renewable technologies and facilitate a transition towards a new energy economy.

1.3 Dissertation Overview

This dissertation will present three pieces of research, all of which have the underlying goal of producing economical solar technologies. The first is focused on the deposition of nanostructured copper sulfide materials in order to create extremely thin

absorber (ETA) devices. The second project discusses the use of inexpensive luminescent downshifting materials to increase the efficiency of CdTe solar cells. The last research project uses computer simulations to investigate the electronic properties of nanocrystalline PbSe solar cell materials.

The remainder of this dissertation is organized as follows. In Chapter 2, a few physical concepts are introduced to provide a foundation for a more technical discussion. This includes the basic theory behind semiconductor materials and solar cell characterization. Chapter 3 will discuss research on nanostructured copper sulfide materials. Chapter 4 will discussion the luminescent downshifting work in detail, and Chapter 5 will discuss the computational PbSe research. Chapter 6 will discuss all three research projects within the context of the solar industry as it currently exists.

Chapter 2

Physical Principles

2.1 Solar Cell Basics

2.1.1 Bands

When atoms are brought into close proximity, individual orbital states can split into two or more distinct states as a consequence of the Pauli exclusion principle. Crystalline solids, containing many atoms in close proximity, have states that are repeatedly split until they effectively form a continuum, or a *band*. Electrons can use unoccupied states to move throughout the material when a band is partially filled, and a solid with a partially filled band is able conduct electric current. In the case of a filled band (i.e. all states are occupied) any flow of charge in the material is negated by an equivalent displacement in the opposite direction. As a result, filled bands cannot produce a current.

The highest occupied band of a material at absolute zero is termed the *valence*

band while the lowest unoccupied band is called the *conduction band*. The energetic distance between the two is called the *band gap*. Metals have a partially filled valence band or a valence band that overlaps with the conduction band. Insulators have a completely filled valence band and a relatively large band gap(>3eV) and have relatively low conductivities. Semiconductors are defined by a filled valence band and a band gap in the range 0.5-3eV.[69]

Semiconductors are particularly useful in solar cells because their band gap energies are comparable to photon energies in the visible portion of the electromagnetic spectrum (the region of maximum irradiance in the solar spectrum). Light that is absorbed by a semiconductor is able to excite electrons into its conduction band, leaving behind positively charged electron voids in the valence band. These voids, called *holes*, behave like positively charged particles that are free to move about the valence band. If these excited electrons and holes, which we collectively refer to as *carriers*, can be redirected through an external circuit en-route to recombining, they can be used to do work. The potential energy gained by the absorption of light and the creation of carriers can be recovered in the circuit as the crystal returns to a more energetically favorable state. This is what happens in a solar cell.

How do we cause electron and hole carriers to detour through a circuit before returning to a relaxed state? The short answer is that we create an electric field inside the solar cell by forming a junction between two semiconductors or between a semiconductor and a metal. The electric field is a result of a transfer of charge that occurs at the interface of the two materials, and it serves to spatially separate excited

electron/hole pairs. This process can be better understood with a brief introduction to Fermi-Dirac statistics.

2.1.2   Fermi-Dirac Statistics/Doping

2.1.2.1   Density of States

Before describing junctions and the transport of electrons and holes in semi-conductor materials, it is necessary to develop a basic understanding of the Fermi-Dirac statistics that determine how carriers distribute themselves among available states. We begin by deriving the *density of states*, or the number of states per unit volume available to carriers at a particular energy (derivation approaches taken from Mackay and Nelson [55, 69]). To calculate the density of states for a 3-D solid we begin by considering the number of states available to a unit volume in k-space, where k_x, k_y, and k_z are the carrier crystal momentum in the x, y, and z directions. Assuming that the wave function solution to the Schrodinger equation for a carrier in a cubic solid is periodic and equal to zero at the boundaries, we can conclude that states available to the carrier are governed by,

$$k_x = \frac{\pi}{L}n_x, \quad k_y = \frac{\pi}{L}n_y, \quad k_z = \frac{\pi}{L}n_z \tag{2.1}$$

where L is the side length of the cubic solid and n_x, n_y, and n_z are integers corresponding to a particular mode. It follows that the number of states per unit k is equal to $\frac{L}{\pi}$ for each direction. The k-space volume per state is $(\frac{\pi}{L})^3$. To calculate the total number of states in a k-space volume, we simply need to divide the total volume by $(\frac{\pi}{L})^3$. Considering

15

only positive momentum, we calculate the area of the sphere of radius k that lies in the k_x, k_y, $k_z > 0$ octant. The number states for a radius k becomes,

$$N = 2 \times \frac{1}{8} \times \frac{4}{3}\pi k^3 \times \left(\frac{L}{\pi}\right)^3 = \frac{1}{3}\frac{L^3}{\pi^2}k^3 \qquad (2.2)$$

By approximating a parabolic relationship between conduction/valence band and crystal momentum,

$$E(\mathbf{k}) = E_{c0} + \frac{\hbar^2\mathbf{k}^2}{2m_c^*} \qquad (2.3)$$

$$E(\mathbf{k}) = E_{v0} - \frac{\hbar^2\mathbf{k}^2}{2m_v^*} \qquad (2.4)$$

where E is the carrier energy, $E_{c0(v0)}$ the bottom (top) of the conduction (valence) band, and $m_{c(v)}^*$ is the effective carrier mass in the conduction (valence) band. It follows that the number states in the energy range, $(E, E + De)$, is given by,

$$\frac{dN}{dE} = \frac{dN}{dk}\frac{dk}{dE} = \frac{L^3}{\pi^2}\frac{\sqrt{2}m_c^{*2/3}}{\hbar^3}\sqrt{E - E_{c0}}, \qquad E > E_{c0} \qquad (2.5)$$

$$\frac{dN}{dE} = \frac{dN}{dk}\frac{dk}{dE} = \frac{L^3}{\pi^2}\frac{\sqrt{2}m_v^{*2/3}}{\hbar^3}\sqrt{E_{v0} - E}, \qquad E < E_{v0} \qquad (2.6)$$

and the density of states is given by,

$$g_c(E) = \frac{dN}{dE}\frac{1}{L^3} = \frac{\sqrt{2}m_c^{*2/3}}{\pi^2\hbar^3}\sqrt{E - E_{c0}}, \qquad E > E_{c0} \qquad (2.7)$$

$$g_v(E) = \frac{dN}{dE}\frac{1}{L^3} = \frac{\sqrt{2}m_v^{*2/3}}{\pi^2\hbar^3}\sqrt{E_{v0} - E}, \qquad E < E_{v0} \qquad (2.8)$$

for the conduction and valence bands respectively. This is the number of states per unit volume available to carriers at a particular energy for a 3D material. Figure 2.1 provides a generic density of states profile based on Equations 2.7 and 2.8.
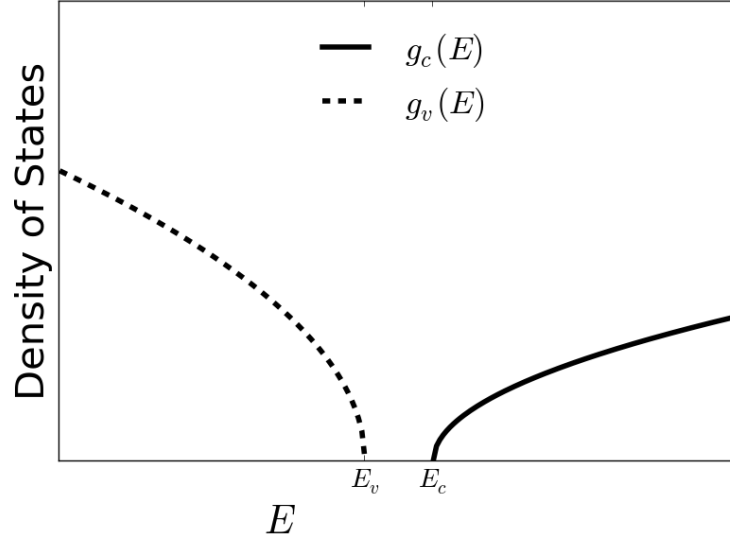
Figure 2.1: Example plots of the density of states solution for a 3D solid (Equations 2.7 and 2.8). Parabola width is determined by the effective mass parameters, m_c^* and m_v^*. The effective mass acts like a free particle mass but is adjusted to account for the periodic potential of the crystal lattice.

The density of sates for materials of fewer dimensions, i.e. a film, rod, or dot can be derived using the same method as carried out for the 3D material. For the purpose of this dissertation, it is worth noting that the density of states for a zero dimensional material, or a quantum dot, consists of atom-like orbital states that can be occupied by electrons of opposite spin.

$$g_{QD}(E) = 2\delta(E - E_0) \tag{2.9}$$

where E_0 is corresponds to the energy level of an orbital. PbSe nanocrystals, which are the focus of Chapter 5, are confined spatially in three dimensions. They therefore exhibit quantized orbital states and serve as a real world example of a quantum dot material.

17

2.1.2.2 Fermi-Dirac Distribution Function

When the density of states is known in addition to the probability of each state being occupied by an electron or hole, we can begin to understand carrier densities, transport, and the the photovoltaic action in solar cell devices. The Fermi-Dirac distribution function provides this probability of occupancy for electrons and holes. To derive the Fermi-Dirac distribution, we consider a system with g_i identical states of energy, E_i, that are occupied by $g_i f_i$ particles, where f_i the probability of a particular state being occupied (derivation taken from [99]). There are

$$W_i = \binom{g_i}{g_i f_i} = \frac{g_i!}{(g_i - g_i f_i)! g_i f_i!} \tag{2.10}$$

possible configurations of $g_i f_i$ particles in g_i states assuming that each state can be occupied by no more than one particle. If more than one energy level is available to the overall system, the total number of configurations, or the *multiplicity*, of the system is given by the product of configurations at each energy level,

$$W = \prod_i W_i \tag{2.11}$$

which can be simplified using Sterling's formula.

$$\ln W = \sum_i \left[g_i \ln g_i - (g_i - g_i f_i) \ln(g_i - g_i f_i) - g_i f_i \ln g_i f_i \right] \tag{2.12}$$

The multiplicity gives us the number of possible configurations for a specific set of occupation probabilities, f_i. Assuming that all configurations are equally probable, the system will naturally reside in the overall state of highest multiplicity at thermal

18

equilibrium. In order to find this state, we introduce the constraints of a constant total energy, U, and total number of particles, N.

$$U = \sum_i E_i g_i f_i \tag{2.13}$$

$$N = \sum_i g_i f_i \tag{2.14}$$

To solve for the thermal equilibrium conditions, we set up the Lagrange function,

$$\Lambda = \ln W - a \sum_j g_j f_j - b \sum_j E_j g_j f_j \tag{2.15}$$

where a and b are Lagrange multipliers corresponding to the constraints of total number of particles and total energy. To solve for thermal equilibrium conditions we find the maxima of our Lagrange function with respect to f_i.

$$\frac{\partial \Lambda}{\partial f_i} = g_i \left(\ln \frac{g_i - g_i f_i}{g_i f_i} - a - bE_i \right) = 0 \tag{2.16}$$

Solving for f_i, we get

$$f_i = \frac{1}{1 + e^{a + bE_i}} \tag{2.17}$$

By reorganizing our Lagrange constants into new constants, E_F and β, this can written as

$$f(E) = \frac{1}{1 + e^{(E - E_f)/\beta}} \tag{2.18}$$

This is the Fermi-Dirac distribution. To avoid a further digression in statistical physics I will leave this derivation at this stage. However, it is important to mention that Equations 2.16 and 2.13, can be compared to the thermodynamic identity,

$$dU = TdS - pdV - \mu dN. \tag{2.19}$$

One finds that $\beta = k_B T$, where k_B is the Boltzmann constant relating temperature, T, to particle energy. E_F is an electrochemical potential, μ, with units of energy that represents how easy or difficult it is to add more particles to the system. In equilibrium, E_F, also called the *Fermi energy*, will be constant everywhere. This concept is very important for the discussion of junctions. Figure 2.2 illustrates the Fermi-Dirac distribution under the conditions, $T = 0$ and $T > 0$.
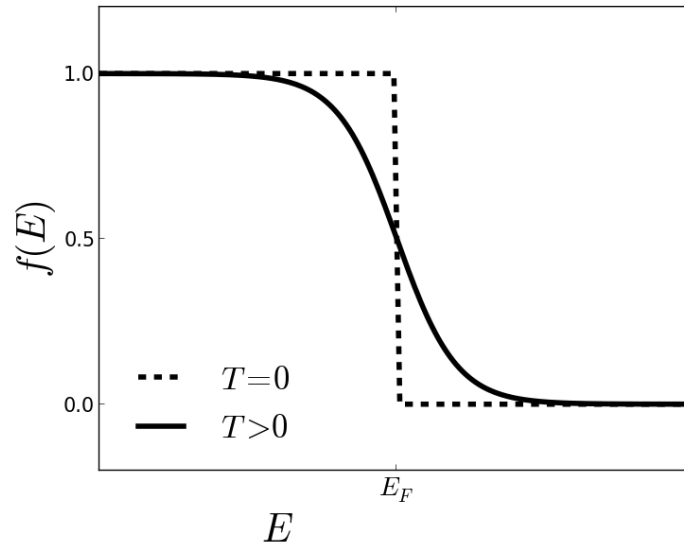
Figure 2.2: Fermi-Dirac distributions at $T = 0$ and $T > 0$. At both temperatures the probability function has a value of $\frac{1}{2}$ when the state energy, E is equal to the Fermi energy, E_F. At $T = 0$ all states below E_F are occupied by electrons while all states above E_F are unoccupied. At $T > 0$, some electrons are thermally excited into states above E_F.

2.1.2.3 Carrier Densities

With the Fermi-Dirac function, we have a tool that describes how likely it is for certain states to be populated. The distribution function can be used in tandem

with knowledge of a material's band structure and density of states to calculate carrier populations in semiconductor solids. The density of electrons in the conduction band is given by

$$n = \int_{E_c}^{\infty} g_c(E) f(E) \, dE \qquad (2.20)$$

for a given Fermi energy, E_F and temperature, T. Because a hole is simply the absence of an electron, we can calculate the hole density in the valence band as

$$p = \int_{-\infty}^{E_v} g_v(E)(1 - f(E)) \, dE. \qquad (2.21)$$

A Fermi energy, E_F, located closer to conduction band will result in a higher concentration of electrons in the conduction band and a lower concentration of holes in the valence band. A material of this type is called an *n-type semiconductor*. If E_F is located closer to the valence band, there will be more mobile holes and fewer mobile electrons. We call this a *p-type semiconductor*. A Fermi level located directly between the two band levels will result in equal concentrations of electron and hole carriers (see Figure 2.3). This is often referred to as an *intrinsic semiconductor*.

These relations apply to semiconductor materials at equilibrium. They also represent a starting point for the analysis of materials that are forced out of equilibrium conditions by an applied bias or by the generation of carriers via light absorption. Solar cell semiconductor layers, which are placed out of equilibrium during device operation, are often approximated using separate, spatially varying Fermi energies for the calculation of electron and hole densities. Under this Quasi Thermal Equilibrium
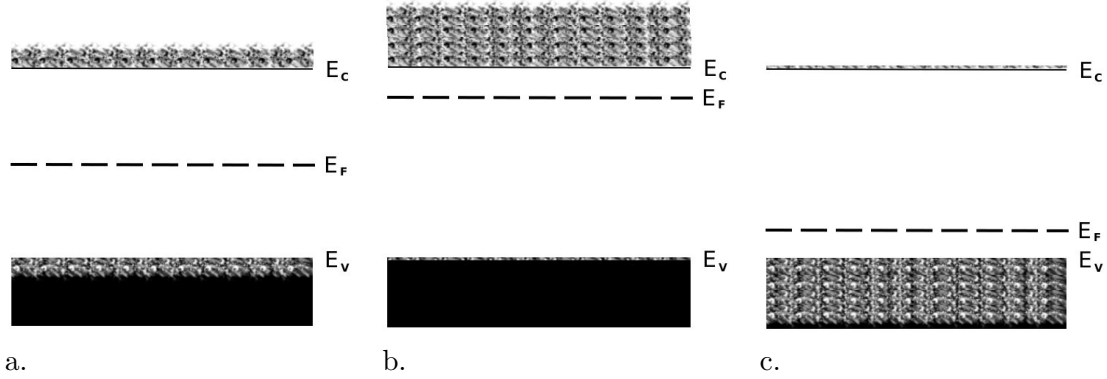
Figure 2.3: Effect of Fermi energy on carrier concentrations. A Fermi energy half way between the conduction and valence bands results in equal concentrations of electrons(black) and holes(white) in the conduction and valence bands, respectively (a). A Fermi energy located close to the conduction band results in a higher concentration of free electrons and a lower concentration of free holes (b). A Fermi energy located close to the valence band results in a higher concentration of free holes and a lower concentration of free electrons (c).

approximation, it can be shown that

$$J_n(\mathbf{r}) = \mu_n n \nabla_{\mathbf{r}} E_{F_n} \tag{2.22}$$

$$J_p(\mathbf{r}) = \mu_p p \nabla_{\mathbf{r}} E_{F_p} \tag{2.23}$$

where μ_n and μ_p are defined as the *electron and hole mobilities*, and E_{F_n} and E_{F_p} are the spatially varying Fermi energies for electrons and holes, respectively. Equations 2.22 and 2.23 give rise to the famous drift-diffusion equations and are used to describe carrier transport in a wide variety of solar cell technologies.

2.1.3 Junctions

In the beginning of this chapter, it was mentioned that a solar cell is able to generate power because it contains an intrinsic electric field that is able to separate

excited electrons and holes. This electric field can be created by forming a junction between semiconductors or between a semiconductor and a metal. This dissertation is primarily concerned with semiconductor-semiconductor junctions, so we will focus our attention on these systems. Consider the band structures of the two semiconductors of similar band gap but different Fermi energies represented in Figure 2.4. The two
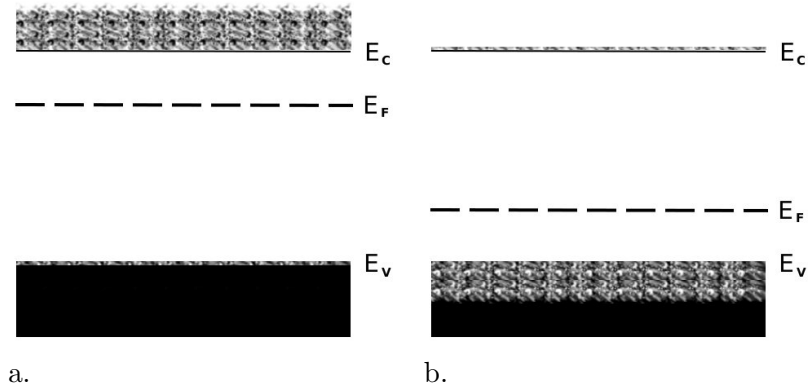
Figure 2.4: Band structures of two semiconductors with roughly the same band gap. Diagram a depicts a n-type semiconductor while diagram b represents a p-type semiconductor.

semiconductors are referenced to a common *vacuum level* (i.e. the energy level corresponding to an electron that is completely free from the crystal). If the two materials were brought into contact with one another the difference in E_F tells us that we will see a redistribution of charge. Electrons will migrate towards the p-type semiconductor and holes will migrate into the n-type material. The carriers meet and combine in the junction region. The redistribution of charge causes the junction region to become charged, and the result is an internal electric field. The electric field creates a change in the vacuum and band levels surrounding the junction, which can be represented in the

23

band diagram (see Figure 2.5) as a gradient in the conduction and valence bands of the two semiconductors. This *band bending* allows the system to reach thermal equilibrium, with no net flow of carriers and a constant Fermi energy throughout the two materials.
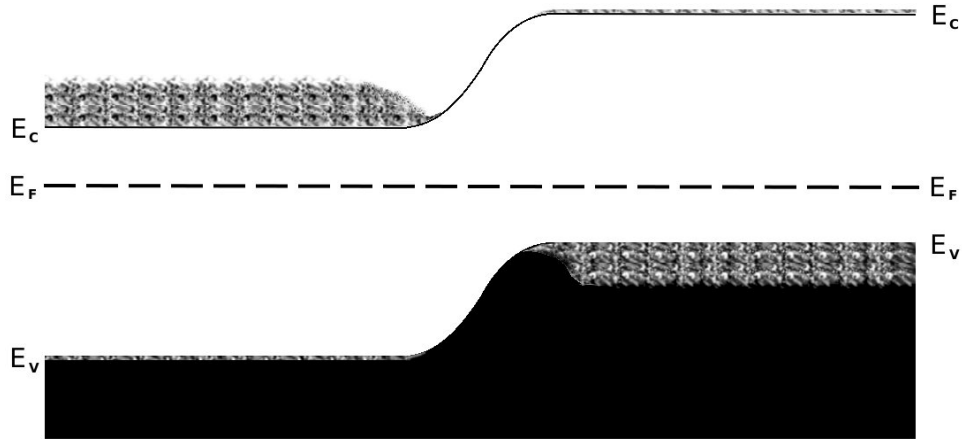
Figure 2.5: Band bending when an n-type and a p-type semiconductor are brought into contact. Charge redistribution results in an internal electric field and a region devoid of majority charge carriers surrounding the junction.

The above example represents a *homojunction*, or a junction between two materials with similar band gaps. When you combine two materials with dissimilar band gaps, it is referred to as a *heterojunction*, and the band diagrams become slightly more complicated. In addition to the field caused by a difference in Fermi energies and the redistribution in charge, there are additional discontinuities in the band diagram that result from the dissimilar band gaps. Because the original materials have different conduction and valence energies, there is an additional energetic boost or penalty incurred when carriers move across the junction. Figure 2.7 shows the original band structures

24

of two materials that can be used to form a heterojunction. For simplicity, we have pre-

served the same difference in Fermi energy levels used in the previous example. When
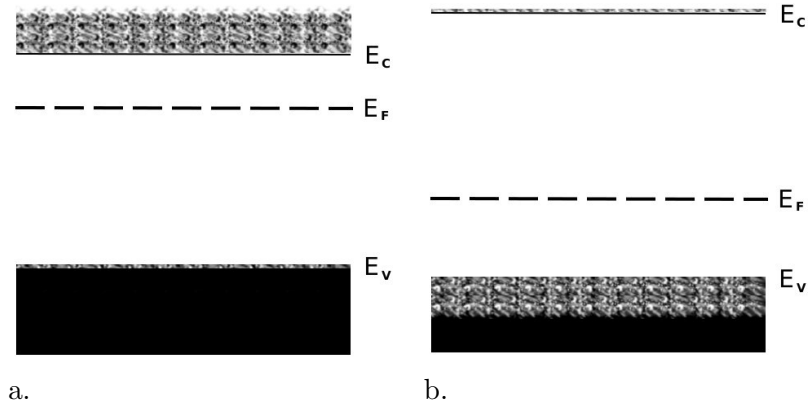
Figure 2.6: Band structures of two semiconductors with dissimilar band gap. Diagram a depicts a n-type semiconductor while diagram b represents a p-type semiconductor.

the two materials are brought together to form a junction, we again see a redistribu-

tion of charge determined by the difference in E_F values. We also see the conduction

and valence bands bend accordingly. Because the p-type material has a larger band

gap, however, the distance between the conduction bands is increased in relation to

the previous example. The difference between the two valence bands is reduced in this

example. The results are discontinuities in the band structure located at the junction.

The conduction band discontinuity encourages the flow of excited electrons towards the

n-type material. In the valence band, it creates a barrier to the flow of holes towards

the p-type material. Such barriers can reduce solar cell efficiency by inhibiting charge

separation at the junction.
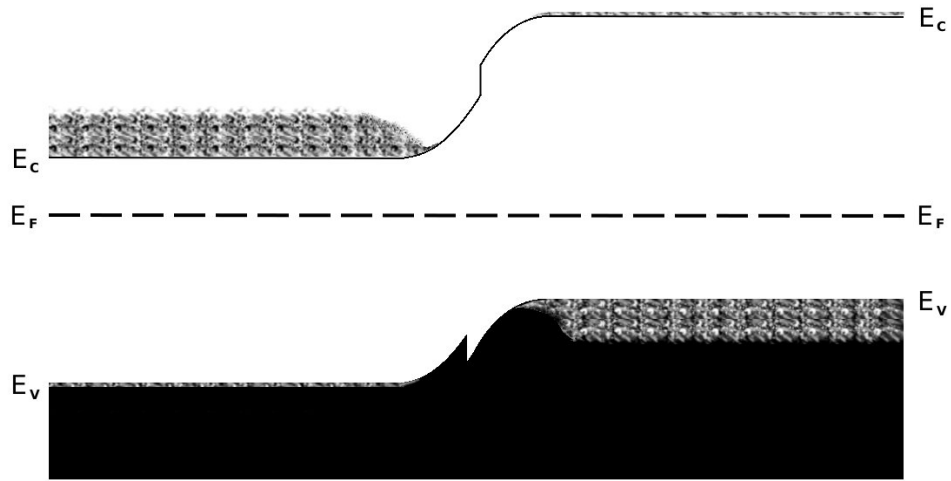
Figure 2.7: Band bending in a semiconductor heterojunction. An additional disconti-
nuity results from the different band gaps of the two materials.

2.1.4   Device Structure

Figure 2.8 depicts a simple solar cell device architecture. The device consists
of four layers. Two layers of semiconductor materials form a heterojunction and are
sandwiched between two electrodes which serve to harvest the photocurrent. Light that
is incident on the solar cell device is absorbed by the semiconductor layers to form
an electron/hole pair, often referred to as an *exciton*. The internal electric field then
separates the exciton such that the electron is diverted toward the anode and the hole
towards the cathode. If the carriers are harvested by the electrodes they can then pass
through an external circuit where they do work en-route to recombining.

A quick note should be made about material considerations when forming the
device contacts. If the anode material is place in contact with an n-type material with
a higher Fermi energy than the metal, we will see the transfer of electrons from the
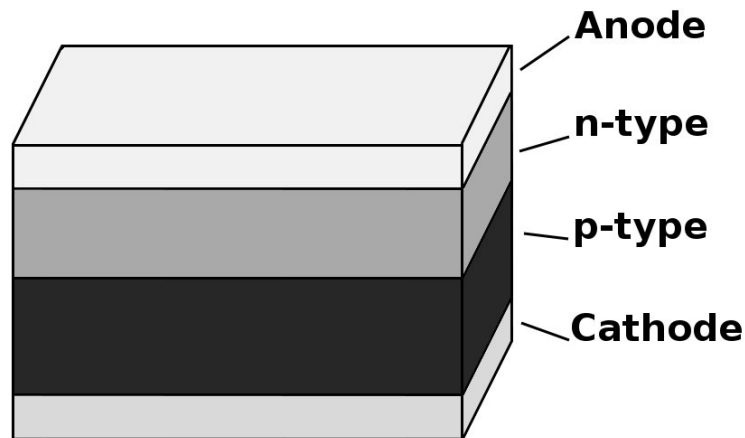
Figure 2.8: Device structure for the simplest form of heterojunction solar cell. The anode is ideally chosen with a lower work function than the n-type material to facilitate charge transport from the semiconductor into the external circuit. Similarly the cathode would ideally have larger work function than the p-type layer.

semiconductor into the electrode. As in the semiconductor junctions described above, this results in an electric field at the junction of the two materials that will impede further electron transport into the metal. An ideal metal contact, therefore, has a higher Fermi energy than the n-type layer to encourage electron flow in what is called an *Ohmic contact*. Using a similar logical progression, it follows that to form an Ohmic contact with the p-type semiconductor, the Fermi level in the metal should have a lower Fermi energy than the p-type material. Another, more common, way to say this is that the anode should have a lower *work function* than the n-type semiconductor and the cathode should have a larger work function than the p-type semiconductor. The work function is simply the measurable distance from the Fermi level to the vacuum level, or the potential required to remove the least tightly bound electron.[69]
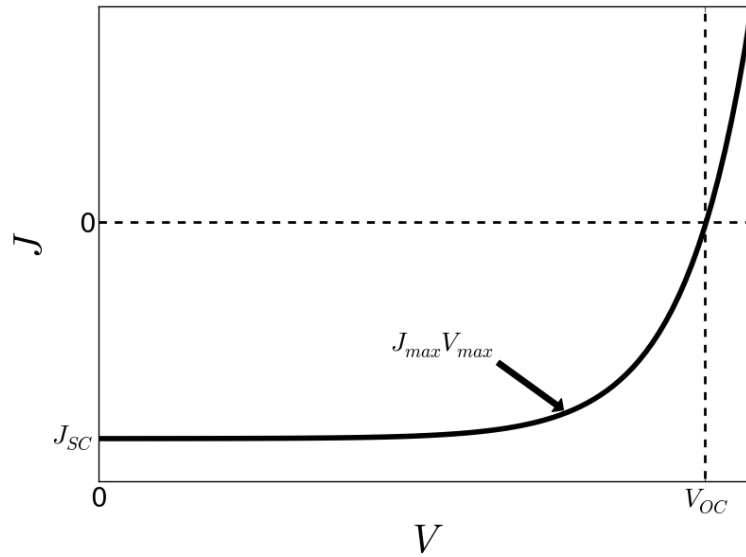
Figure 2.9: Sample current-voltage characteristic for a solar cell. The open circuit voltage, V_{OC}, and the short circuit current, J_{SC} are indicated on the axes. The point of maximum power generation is labeled as $J_{max}V_{max}$.

2.1.5 Characterization

When a solar cell is placed in the sunlight, it will be able to generate a *photocurrent* through some external circuit. It will also produce a *photovoltage*, which is related to the resistance of the circuit. It is the measurement of these values that allows researchers to evaluate the performance of a particular solar cell. Figure 2.9 provides an example current-voltage characteristic, which shows the photocurrent density produced when the solar cell electrodes are held at a particular potential difference.

Imagine a solar cell connected to some external circuit with very low resistance. Light will come in and carriers will be excited and separated in the solar cell. They are then able to easily recombine by passing through the circuit. Under these conditions the

28

solar cell will produce a high photocurrent density, but carriers are only required to do minimal work in order to recombine. This configuration will produce a low photovoltage across the circuit. The power density is given as the product of the photocurrent density, J, and the photovoltage, V, across the circuit, and under these conditions, the power generated by the solar cell will be relatively low. The photocurrent of a solar cell when its terminals are held at zero bias is an important parameter used in solar cell characterization call the short circuit current, J_{SC}.

At the other extreme, we can consider an solar cell connected to a circuit of relatively high resistance. Every carrier that is able to navigate through the circuit is able to do a relatively large amount of work. However, because the circuit has become more difficult to navigate, the photocurrent is reduced. The bias at which there is no photocurrent produced is another important parameter called the open circuit voltage V_{OC}.

Somewhere in between these two extremes, there exists a point where the photocurrent and the photovoltage are both significant and the solar cell is able to produce the maximum amount of power. This is called the maximum power point, and it is characterized by the values J_{max} and V_{max}. This point is indicated by the arrow in Figure 2.9. Solar cell efficiency is calculated as

$$\eta = \frac{J_{max}V_{max}}{P}, \tag{2.24}$$

where P is power contained in the incident electromagnetic spectrum.

The last characterization parameter we will mention in this section is called the

fill factor, FF. It serves as a measure "squareness" in the current-voltage characteristic. In other words it describes how close J_{SC} and V_{OC} are to J_{max} and V_{max}.

$$FF = \frac{J_{max}V_{max}}{J_{SC}V_{OC}}.$$

(2.25)

Solar cell efficiency can also be written as

$$\eta = \frac{J_{SC}V_{OC}FF}{P},$$

(2.26)

in terms of J_{SC}, V_{OC}, and FF.

2.2 Optical Principles

Maxwell's equations provide a theoretical foundation for the description of electromagnetic waves and device optics. The following derivation of the Helmholtz wave equations is adapted from the work of Griffiths.[31] In a dielectric medium with no free charge or current, Maxwell's equations are given by

i) $\nabla \cdot \mathbf{D} = 0$ iii) $\nabla \times \mathbf{E} = -\dfrac{\partial \mathbf{B}}{\partial t}$

ii) $\nabla \cdot \mathbf{B} = 0$ iv) $\nabla \times \mathbf{H} = \dfrac{\partial \mathbf{D}}{\partial t}$,

(2.27)

where

$$\mathbf{D} = \epsilon \mathbf{E} \qquad \text{and} \qquad \mathbf{H} = \frac{1}{\mu}\mathbf{B}.$$

(2.28)

E and B are the electric and magnetic fields, respectively, and ϵ and μ are the permittivity and the permeability of the material. If we combine Equations 2.27 iii and

iv, we can form an important differential equation,

$$\nabla \times (\nabla \times \mathbf{E}) = -\epsilon\mu\frac{\partial^2 \mathbf{E}}{\partial t^2} \tag{2.29}$$

Using the mathematical relation, $\nabla \times (\nabla \times \mathbf{A}) = \nabla(\nabla \cdot \mathbf{A}) - \nabla^2\mathbf{A}$, we get

$$\nabla(\nabla \cdot \mathbf{E}) - \nabla^2\mathbf{E} = -\epsilon\mu\frac{\partial^2 \mathbf{E}}{\partial t^2}$$

$$\nabla^2\mathbf{E} = \epsilon\mu\frac{\partial^2 \mathbf{E}}{\partial t^2} \tag{2.30}$$

using Equation 2.27 i. Similarly, we could just as easily combine equations iii and iv in terms of $\mathbf{B}$ to get the result,

$$\nabla(\nabla \cdot \mathbf{B}) - \nabla^2\mathbf{B} = -\epsilon\mu\frac{\partial^2 \mathbf{B}}{\partial t^2}$$

$$\nabla^2\mathbf{B} = \epsilon\mu\frac{\partial^2 \mathbf{B}}{\partial t^2} \tag{2.31}$$

The results 2.30 and 2.30 take the form of familiar Helmholtz wave equation with plane wave solutions,

$$\mathbf{E} = \mathbf{E_0}e^{i(k\mathbf{u}\cdot\mathbf{r}-\omega t)}$$

$$\mathbf{B} = \mathbf{B_0}e^{i(k\mathbf{u}\cdot\mathbf{r}-\omega t)}, \tag{2.32}$$

where $\mathbf{u}$ is a unit vector defining the the direction of wave propagation. The following relations also hold:

$$k^2 = \epsilon\mu\omega^2 \tag{2.33}$$

$$n = c/v = \frac{k}{\omega}c = \sqrt{\frac{\epsilon\mu}{\epsilon_0\mu_0}}. \tag{2.34}$$

k determines the spatial frequency of the wave oscillation, and ω determines the temporal frequency of the oscillation. They are related to each other by a factor, $\sqrt{\epsilon\mu}$, which

is the inverse of the speed of propagation in the material, v. n is the index of refraction of the material.

2.2.1 Absorption

Now as a slightly more complicated example, consider a dielectric medium in which the electrons are bound to their positively charged ions by harmonic forces (derivation borrowed from Huang[33]). The polarization is defined as the dipole moment per unit volume,

$$P = n_0 d = n_0 e x, \tag{2.35}$$

where P is the polarization, $d =$ is the electric dipole moment, n_0 is the density of electrons, e is the charge of an electron, and x is the electron displacement. If we describe the displacement of an electron in an oscillating electric field, $E(t)$, as a damped, driven oscillator we get,

$$m_0 \frac{d^2 x}{dt^2} = -2m_0 \gamma \frac{dx}{dt} - m_0 \omega_0^2 x + eE(\omega)e^{-i\omega t} \tag{2.36}$$

with the solution,

$$x(t) = x(\omega)e^{-i\omega t} = \frac{-eE(\omega)}{m_0(\omega^2 + i2\gamma\omega - \omega_0^2)} e^{-i\omega t}. \tag{2.37}$$

Here m_0 is the electron mass, ω_0 is the non-perturbed oscillation frequency, and ω is the frequency of $E(t)$. Combining Equations 2.35 and 2.37 we get,

$$P(\omega) = \frac{-n_0 e^2 E(\omega)}{m_0(\omega^2 + i2\gamma\omega - \omega_0^2)}. \tag{2.38}$$

32

The coefficient relating the polarization amplitude, $P(\omega)$, to the electric field amplitude, $E(\omega)$, is called the optical susceptibility,

$$\chi(\omega) = \frac{-n_0 e^2}{m_0(\omega^2 + i2\gamma\omega - \omega_0^2)} \tag{2.39}$$

$$= \frac{-n_0 e^2}{2m_0\omega_0'} \left(\frac{1}{\omega - \omega_0' + i\gamma} - \frac{1}{\omega - \omega_0' + i\gamma} \right). \tag{2.40}$$

Here we have rewritten,

$$\omega_0' = \sqrt{\omega_0 - \gamma} \tag{2.41}$$

χ is related to the material's dielectric constant, ϵ by

$$\epsilon(\omega) = 1 + \chi(\omega). \tag{2.42}$$

We can see that we must consider complex values of ϵ in dielectric material.

$$\epsilon = \epsilon' + i\epsilon'' \tag{2.43}$$

If we assume that we are very close to resonance, we can write,

$$\epsilon = 1 - \frac{n_0 e^2}{2m_0\omega_0'} \frac{1}{\omega - \omega_0' + i\gamma} \tag{2.44}$$

$$\epsilon' = 1 - \frac{n_0 e^2}{2m_0\omega_0'} \frac{\omega - \omega_0'}{(\omega - \omega_0')^2 + \gamma^2} \tag{2.45}$$

$$\epsilon'' = \frac{n_0 e^2}{4m_0\omega_0'} \frac{2\gamma}{(\omega - \omega_0')^2 + \gamma^2}. \tag{2.46}$$

To see what this means for electromagnetic waves in dielectric media, consider Equation 2.33 with a complex ϵ.

$$(k' + ik'')^2 = (\epsilon' + i\epsilon'')\mu\omega^2. \tag{2.47}$$

33
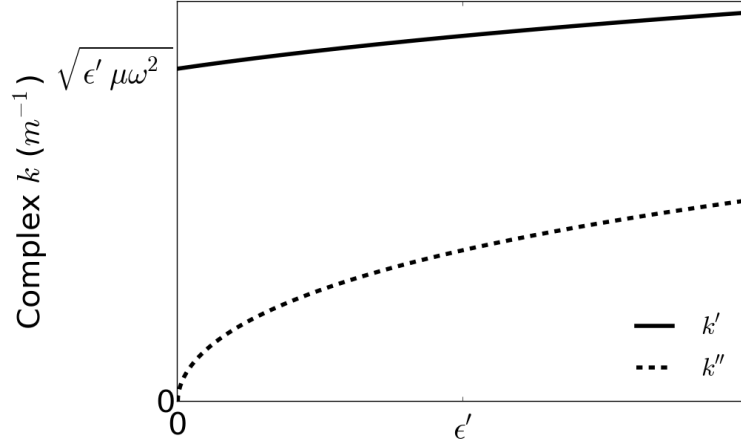
Figure 2.10: Real and imaginary components of the wave number in the harmonic oscillator model for dielectrics. The real component k', is closely related to the material's index of refraction, n, while the imaginary component, k'', closely related to the material's absorption coefficient.

We can solve for the real and imaginary components of k,

$$k' = \left(\frac{\epsilon' \mu \omega^2}{2} \left(\sqrt{1 + \frac{\epsilon''^2}{\epsilon'^2}} + 1 \right) \right)^{\frac{1}{2}} \tag{2.48}$$

$$k'' = \left(\frac{\epsilon' \mu \omega^2}{2} \left(\sqrt{1 + \frac{\epsilon''^2}{\epsilon'^2}} - 1 \right) \right)^{\frac{1}{2}}. \tag{2.49}$$

The following relation also holds,

$$k'' = \frac{\mu \omega^2}{2k'} \epsilon''. \tag{2.50}$$

If we plug our complex k back into the solutions 2.32, the complex component of k give rise to exponential decay terms,

$$\mathbf{E} = \mathbf{E_0} e^{i(k' \mathbf{u} \cdot \mathbf{r} - \omega t)} e^{-k'' \mathbf{u} \cdot \mathbf{r}} \tag{2.51}$$

$$\mathbf{B} = \mathbf{B_0} e^{i(k' \mathbf{u} \cdot \mathbf{r} - \omega t)} e^{-k'' \mathbf{u} \cdot \mathbf{r}}, \tag{2.52}$$

34

This wave attenuation is the absorption of light by our dielectric material.

We define the absorption coefficient, α, as the parameter used to characterize a material's light absorption.

$$\alpha = 2k''. \tag{2.53}$$

$1/\alpha$ defines the distance a wave must travel in the host material such that its intensity, $I \propto |E|^2$, decreases by $1/e$.

When calculating the index of refraction, n, we now consider the real component of k,

$$n = \frac{k'}{\omega}c. \tag{2.54}$$

The Beer-Lambert law follows from Equations 2.51-,

$$\boxed{I = I_0 e^{-\alpha l},} \tag{2.55}$$

for light traveling through a material of thickness l. I is light intensity at material depth, l, and I_0 is the original light intensity before absorption. This is an important result for the experimental data presented in the next two chapters.

2.2.2 Reflection/Refraction

Going back to Maxwell's equations, we can extract more information concerning electromagnetic wave properties and describe reflection and refraction phenomena (the following is borrowed from Griffiths and Jackson [31, 39]). Applying Equations 2.27 i and ii to Equations 2.32, we can see that

$$\mathbf{u} \cdot \mathbf{E} = 0 \qquad \text{and} \qquad \mathbf{u} \cdot \mathbf{B} = 0. \tag{2.56}$$

35

This means that $\mathbf{E}$ and $\mathbf{B}$ run perpendicular to the direction of wave propagation. From Equations 2.27 iii and iv, it can be deduced that,

$$\mathbf{B} = \frac{k}{\omega}\mathbf{u} \times \mathbf{E}. \tag{2.57}$$

$\mathbf{E}$ and $\mathbf{B}$ run perpendicular to each other as well.

Now consider the situation in which an electromagnetic wave encounters a boundary between two dielectric materials with indices of refraction, n_1 and n_2 and dielectric constants ϵ_1 and ϵ_2. We assume that solution will consist of up to three waves; an incident wave in the n_1 medium,

$$\mathbf{E_I} = \mathbf{E_{I_0}}e^{i(k_I \mathbf{u_I} \cdot \mathbf{r} - \omega t)} \qquad \text{and} \qquad \mathbf{B_I} = \frac{k_I}{\omega}\mathbf{u_I} \times \mathbf{E_I}, \tag{2.58}$$

a reflected wave also in the n_1 region,

$$\mathbf{E_R} = \mathbf{E_{R_0}}e^{i(k_R \mathbf{u_R} \cdot \mathbf{r} - \omega t)} \qquad \text{and} \qquad \mathbf{B_R} = \frac{k_R}{\omega}\mathbf{u_R} \times \mathbf{E_R}, \tag{2.59}$$

and a transmitted/refracted wave in the n_2 medium,

$$\mathbf{E_T} = \mathbf{E_{T_0}}e^{i(k_T \mathbf{u_T} \cdot \mathbf{r} - \omega t)} \qquad \text{and} \qquad \mathbf{B_T} = \frac{k_T}{\omega}\mathbf{u_T} \times \mathbf{E_T}. \tag{2.60}$$

The frequency, ω, is a property inherent to the wave and remains the same in all three media, so we have

$$\omega = \frac{k_I}{n_1} = \frac{k_R}{n_1} = \frac{k_T}{n_2} \qquad \text{and} \qquad k_I = k_R = \frac{n_1}{n_2}k_T. \tag{2.61}$$

Because the boundary conditions for the wave solution must hold at all points on the plane at all times, the exponentials in Equations 2.58-2.60 must be in phase at

36

the boundary, which we define by $z = 0$. It follows that,

$$(k_I \mathbf{u_I} \cdot \mathbf{r})_{z=0} = (k_R \mathbf{u_R} \cdot \mathbf{r})_{z=0} = (k_T \mathbf{u_T} \cdot \mathbf{r})_{z=0}$$

$$= k_I \sin(\theta_I) = k_R \sin(\theta_R) = k_T \sin(\theta_T), \tag{2.62}$$

where $\theta_{I,R,T}$ corresponds to angular deviation from the vector normal to the boundary of the two materials Since, $k_I = k_R$, we know $\theta_I = \theta_R$, and we arrive at Snell's law.

$$\theta_I = \theta_R \qquad \text{and} \qquad \boxed{n_1 \sin(\theta_I) = n_2 \sin(\theta_T)} \tag{2.63}$$

Equation 2.63 allows us to calculate the critical angle $\theta_c = \sin^{-1}(\frac{n_1}{n_2})$ at which incident light is completely reflected at the boundary of two materials. The concept of *total internal reflection* is important in the design of Extremely Thin Absorber solar cells, which are discussed later in Chapter 3. Considering the situations in which $x = 0$ and $y = 0$ we can also conclude from Equation 2.62 that $\mathbf{u_I}$, $\mathbf{u_R}$, and $\mathbf{u_T}$ all lie in the same plane, which we will term the *plane of incidence*.

The integral forms of Maxwell's equations, give rise to boundary conditions at the junction of two distinct materials,

i) $[\epsilon_1(\mathbf{E_{I_0}} + \mathbf{E_{R_0}}) - \epsilon_2 \mathbf{E_{T_0}}] \cdot \mathbf{n} = 0$

iii) $[k_I \mathbf{u_I} \times \mathbf{E_{I_0}} + k_R \mathbf{u_R} \times \mathbf{E_{R_0}} - k_T \mathbf{u_T} \times \mathbf{E_{T_0}}] \cdot \mathbf{n}$

ii) $(\mathbf{E_{I_0}} + \mathbf{E_{R_0}} - \mathbf{E_{T_0}}) \times \mathbf{n}$

iv) $\left[\dfrac{1}{\mu_1}(k_I \mathbf{u_I} \times \mathbf{E_{I_0}} + k_R \mathbf{u_R} \times \mathbf{E_{R_0}}) - \dfrac{1}{\mu_2} k_T \mathbf{u_T} \times \mathbf{E_{T_0}} \right] \times \mathbf{n}, \tag{2.64}$

where $\mathbf{n}$ is a unit vector, normal to the plane formed by the junction of the two materials.[39] Based on these boundary conditions, we can determine the amplitudes

the the transmitted and reflected waves at any angle of incidence, θ_I. It is easiest to consider two special cases; when the electric field of the incident wave is perpendicular to the plane of incidence and when the electric field is parallel to the plane of incidence. In the first of these two cases, we have $\mathbf{E_0} \cdot \mathbf{n} = 0$ and $\mathbf{u} \times \mathbf{E_0} \cdot \mathbf{n} = 0$ for all three waves. Two equations result from applying these condition to Equations 2.64:

$$E_{I_0} + E_{R_0} - E_{T_0} = 0 \tag{2.65}$$

$$\sqrt{\frac{\epsilon}{\mu}}(E_{I_0} - E_{R_0})\cos(\theta_I) - \sqrt{\frac{\epsilon'}{\mu'}}E_{T_0}\cos(\theta_T) = 0 \tag{2.66}$$

These results lead to the following amplitudes for our reflected and transmitted waves:

$$\boxed{\frac{E_{R_0}}{E_{I_0}} = \frac{n_1\cos(\theta_I) - \frac{\mu}{\mu'}\sqrt{n_2^2 - n_1^2\sin^2(\theta_I))}}{n_1\cos(\theta_I) + \frac{\mu}{\mu'}\sqrt{n_2^2 - n_1^2\sin^2(\theta_I))}}} \tag{2.67}$$

$$\boxed{\frac{E_{T_0}}{E_{I_0}} = \frac{2n_1\cos(\theta_I)}{n_1\cos(\theta_I) + \frac{\mu}{\mu'}\sqrt{n_2^2 - n_1^2\sin^2(\theta_I))}}} \tag{2.68}$$

A similar approach is used in the situation where the electric field is parallel to the plane of incidence. Equations 2.64 iii and iv give rise to the equalities,[39]

$$\cos(\theta_I)(E_{I_0} - E_{R_0}) - \cos(\theta_T)E_{T_0} = 0 \tag{2.69}$$

$$\sqrt{\frac{\epsilon}{\mu}}(E_{I_0} + E_{R_0}) - \sqrt{\frac{\epsilon'}{\mu'}}E_{T_0} = 0, \tag{2.70}$$

leading to,

$$\boxed{\frac{E_{R_0}}{E_{I_0}} = \frac{\frac{\mu}{\mu'}n_2^2\cos(\theta_I) - n_1\sqrt{n_2^2 - n_1^2\sin^2(\theta_I)}}{\frac{\mu}{\mu'}n_2^2\cos(\theta_I) + n_1\sqrt{n_2^2 - n_1^2\sin^2(\theta_I)}}} \tag{2.71}$$

$$\boxed{\frac{E_{T_0}}{E_{I_0}} = \frac{2n_1n_2\cos(\theta_I)}{\frac{\mu}{\mu'}n_2^2\cos(\theta_I) + n_1\sqrt{n_2^2 - n_1^2\sin^2(\theta_I)}}} . \tag{2.72}$$

38

Equations 2.67-2.72 are called the Fresnel formulas for reflection and refraction, and they allow us to describe light scattering and absorption throughout semiconductor materials and solar cell devices. Figure 2.11 shows $\frac{E_{R_0}}{E_{I_0}}$ as a function of θ_I.
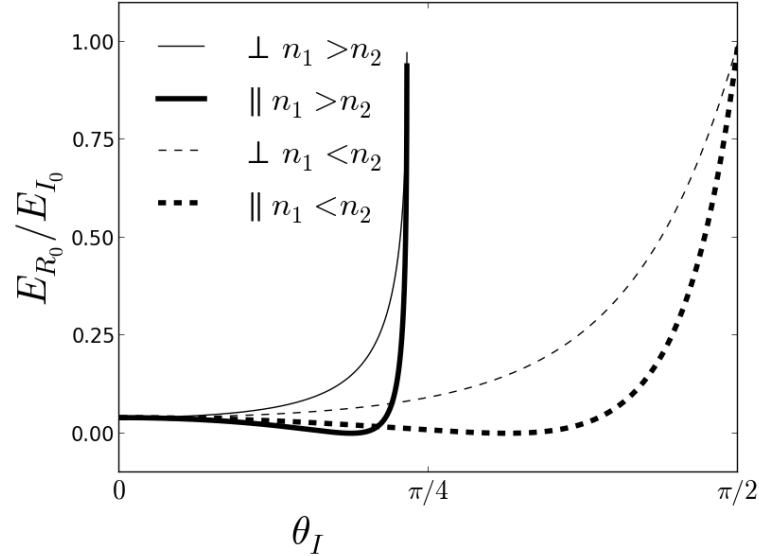
Figure 2.11: Reflection coefficient with angle of incidence for light traveling from a medium of n_1 into a medium of n_2. Perpendicular and parallel polarized light are both considered. Light is traveling from a more dense medium into a lighter medium is completely reflected at angles beyond the critical angle.

2.2.3 Light Management

When designing a solar cell device, we consider the optical properties of the materials in order to maximize the efficiency and minimize the cost of the device. In general, it makes sense to try and absorb as much sunlight as possible while using as little material as possible. Referring back to Equation 2.55, we can see that to increase light absorption, we can use materials with larger absorption coefficients, α, or we

increase the path length of the light through the absorbing layers. The latter approach is emphasized in the extremely thin absorber (ETA) solar cell by incorporating a highly structured heterojunction boundary.[44, 27, 91].
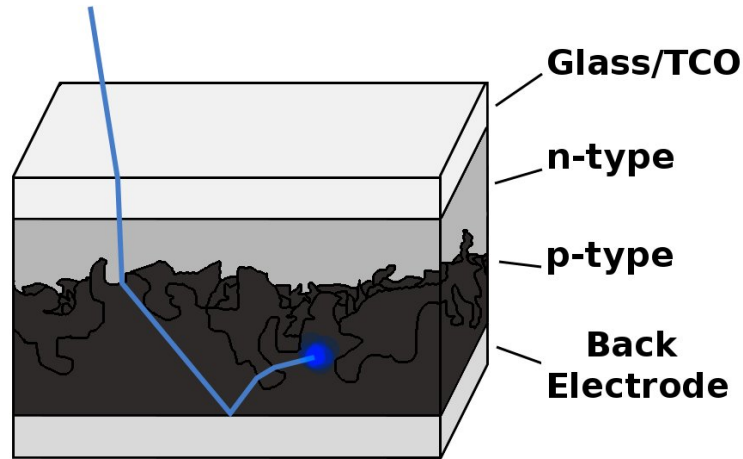
Figure 2.12: Absorption in an ETA solar cell. Light enters through the glass and transparent conductive oxide layer facing the light source. Light is heavily scattered by the highly structures interface at the heterojunction boundary thus increasing its path length through the absorbing layer.

Figure 2.12 represents one approach towards designing an ETA solar cell. Light incident on the solar cell enters through the glass substrate which is coated with a transparent conducting oxide film to serve as the front contact. The majority of the transmitted light then propagates into a mostly transparent n-type window layer. As the light encounters each material boundary, its transmission efficiency governed by equations 2.67-2.72, and its propagation angle is determined by Equation 2.63. Light is scattered again at the boundary between the window layer and the absorbing p-type layer, but because the boundary between the two semiconductor layers has been highly structured, light is often scattered at extreme angles. Light that reached the back

contact may be reflected, after which, it passes back through the absorbing layer and is refracted again at the interface of the window and absorbing materials. Scattering at nanostructured heterojunction can increase the optical path length of the light through the absorbing layer by a factor of five.[27]

The increased optical path of the ETA absorbing layer yields two major benefits. Increased absorption means that thinner absorbing layers may be used. This translates into lower materials and manufacturing costs. Secondly, thinner absorbing layers mean more efficient carrier collection at the electrodes due to shorter transport distances. The work presented in Chapter 3 is a step towards developing Cu_2S materials for the fabrication of ETA solar cells

Chapter 4 highlights another approach to light management in solar cell devices. From the harmonic oscillator treatment of absorption in Section 2.2.1, one recalls that the dielectric constant, ϵ, and the absorption coefficient, α, are wavelength specific. Consequently, materials often absorb some light frequencies better than others, and light-converting solar cell layers perform better in certain regions of the electromagnetic spectrum. In some regions of the incident spectrum, device encapsulants, contacts, and window layer materials might also absorb some of the light that could otherwise be converted in to electricity in a process called *parasitic absorption*. In general, solar cell performance depends strongly on the incident spectrum. One approach to improving device performance is to adjust the incident spectrum using luminescent downshifting films. Figure 2.13 illustrates this approach.

When a luminescent material absorbs strongly at a particular frequency of

41
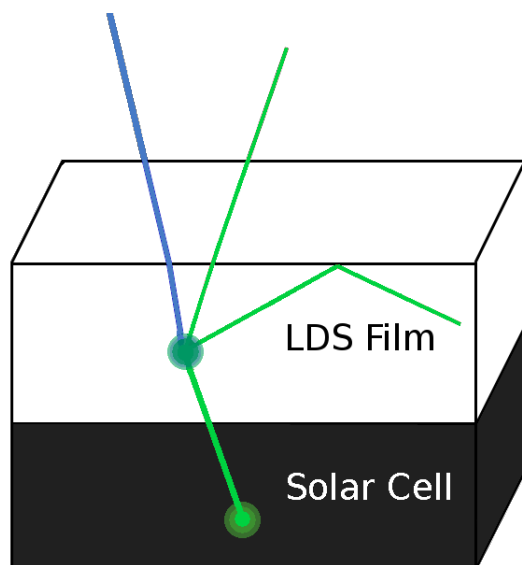
Figure 2.13: Light management using a luminescent downshifting film. The organic luminescent film is placed above the solar cell so as to alter the spectrum received by the device.

light, that frequency often corresponds to a particular electron transition in that material. When that transition relaxes, light is often re-emitted at that same frequency. However, in some luminescent materials, the chemical structure of the absorbing material will change as a result of being in an excited state. Energy is lost in the chemical change, and these materials will re-emit light at a frequency that is lower than the light that was absorbed. The energy difference between the absorbed and radiated light in organic materials is called a *Stokes shift*,[50] and it provides a useful tool for *downshifting* light. In Chapter 4, luminescent materials are developed to absorb in certain regions of the solar spectrum and to re-emit light in regions better suited to device performance. These materials are then incorporated in the solar cell device so that the active device materials are exposed to an altered spectrum.

Chapter 3

Deposition of Cu$_2$S for ETA Solar Cells

3.1 Motivation

3.1.1 ETA Cells

The extremely thin absorber (ETA) cell is a solar cell concept that utilizes a highly-structured heterojunction to scatter light, thus increasing the effective thickness of the absorbing layer.[27] By allowing for thinner absorbing layers, these devices also reduce the transport path for excited charge carriers. A challenge in the development of solid state ETA devices is finding an effective technique for the deposition of semiconducting materials within nanoporous structures to form an inter-penetrating junction. Chemical vapor deposition (CVD) is a gas-phase deposition process that can penetrate into pores as small as 4nm in diameter,[41] making it a promising tool for fabricating ETA solar cells. This article characterizes Cu$_x$S films deposited by pulsed chemical vapor deposition (PCVD) on porous nanocrystalline TiO$_2$ and planar ZnO for future

applications in photovoltaics.

3.1.2 Cu_2S

Cu_2S was a leading thin-film solar cell material in the 1980s due to its indirect band gap near 1.2eV and to its relative abundance and non-toxicity. Cu_2S/CdS devices achieved an efficiency of 9.1%. However, the diffusion of copper ions across the Cu_2S/CdS boundary severely limits the lifetime of this device structure.[10, 5] Porous nanocrystalline TiO_2 has been established as an effective dye sensitized solar cell material. In addition, TiO_2 exhibits superior chemical stability and is expected to form a robust junction when paired with Cu_2S.[77, 53] ZnO is another stable semiconductor that has also been proposed as a window layer material in Cu_2S devices. Theoretical work has shown that Cu_2S/ZnO devices should have higher open circuit voltages and collection efficiencies than comparable Cu_2S/CdS devices.[13]

3.1.3 PCVD

In both PCVD and CVD, substrates under vacuum are exposed to gaseous precursors containing the constituents of a desired deposition product. A chemical reaction is initiated at or near the substrate's surface, producing the desired material on the substrate. In CVD, the substrate is continuously exposed to both precursors at the same time. PCVD uses a stepwise injection process in which the substrate is separately exposed to each precursor in a series of pulses and purges inside a deposition chamber. PCVD is analogous to atomic layer deposition (ALD) except for the fact

that the purge steps are relatively short, and it is possible that the reaction chamber still contains gaseous precursor after the purge steps. For PCVD, a single exposure cycle results in the precursor-limited deposition of a highly conformal layer of material. Precise control over film thickness is obtained by controlling the number of cycles used in the process. For all CVD processes, the morphology of the deposited material is largely affected by the nature of the chemical reaction, the conditions inside the deposition chamber, and surface chemistry of the substrate.

3.1.4 KI5

Copper sulfides are known to exist in eight stoichiometric phases ranging from copper-rich Cu_2S (chalcocite) to copper-poor CuS (covellite).[65, 19] Aside from the chalcocite phase, these crystal phases are too conductive to be used as absorbing layers in solar cell devices. Previous work using ALD and $Cu(thd)_2$ as the copper precursor yielded $Cu_{1.8}S$ or CuS depending on the substrate temperature during the deposition.[78, 79, 42] Other ALD work successfully produced Cu_2S using bis(N , N' - di-sec-butylacetamidinato)dicopper(I) as the copper precursor.[58] This article presents Cu_xS materials deposited using KI5, a new precursor that has been previously used for the deposition of copper. KI5 is a fluorine-free molecule based on the common Cu(hfac)(tmvs) precursor also known as CupraSelect14. The chemical structure of KI5 contains a seven member ring that imparts greater thermal stability, allowing for high vapor pressures (>2Torr at 140C) and deep penetration into highly structured surfaces.[70] In addition, this precursor avoids fluorine impurities resulting from precur-

sor decomposition.

3.2 Experimental Work

A custom built reactor was used for the deposition of Cu_xS. The reactor was a single wafer chamber with two separately controlled injectors to introduce KI5 and hydrogen sulfide either simultaneously for CVD deposition or as alternating pulses for PCVD deposition. The reaction zone was confined in a parallel plate configuration between a 200mm heated substrate chuck and a 200mm heated shield 20mm above the substrate chuck. The copper precursor was heated to 90°C and all gas lines between the reactor, injectors and heat shield were heated to temperatures in the range, 90-100C. Outside of the reaction zone was a second shield at ambient temperature. The substrates were 1 square substrates placed directly under the injectors. The chamber base pressure prior to deposition was 10-6 Torr. Nitrogen (>99% pure) was used as the carrier/purge gas for both the KI5 and H_2S. The PCVD timing sequence consisted of a 3 second N_2 purge followed by a 5 second H_2S exposure, another 3 second purge, and finally a 12 second KI5 exposure. The chamber pressure was maintained at 0.3 Torr during the KI5 and between 0.3-0.6 Torr during the H_2S exposure. The chamber pressure during CVD depositions ranged between 0.7 and 0.9 Torr. For both processes, H_2S was formed in-situ by reacting Al_2S_3 powder with water. The H_2S gas was passed through a powder desiccant to reduce residual water to less than 1%. A quadrupole mass spectrometer was used to monitor the purity of the H_2S reaction gas and reaction

46

byproducts.

A hydrophilic substrate with a suitable electron valence state was necessary for a successful Cu_xS PCVD deposition. Depositions were attempted on Corning glass, sol-gel deposited TiO_2, sintered 100nm TiO_2 nanoparticles, and sol-gel deposited ZnO. Of these substrates, only the 100nm TiO_2 nanoparticles and sol-gel ZnO yielded Cu_xS from the PCVD process. The PCVD films on ZnO and TiO_2 were very uniform across the 1 substrate. The CVD process yielded Cu_2S films on all substrate types independent of substrate temperature, and CVD films were very non-uniform, forming only directly below the injectors. These results indicate a gas phase reaction during the CVD process rather than a reaction at the substrate's surface. The nanostructured TiO_2 films were made by spin-casting a commercial solution of suspended TiO_2 nanoparticles (Solaronex), annealing in a vacuum oven for 1 hour at 110°C and sintering the film in air for 10 minutes at 450C. The ZnO sol-gel process was adapted from from a process illustrated in detail by Jim-Hong Lee et al.[52] Zinc acetate was dissolved in a mixture of 2-methoxyethanol and monoethanolamine at room temperature. The mixture was then stirred at 60°C for 2hrs. Films were then spin cast and the solvent was evaporated on a hot plate for 10min. The sol-gel films were then annealed in a vacuum at 110°C for 1hr. and sintered in a tube furnace in air for 1 hour at 450°C.

3.3 Results

3.3.1 PCVD Results

In previous work using atomic layer deposition (ALD) with $Cu(thd)_2$ as the Cu precursor, a drop in the measured growth rate at the transition temperature (180C) distinguished two deposition regimes of Cu_xS crystal phases.[78] The PCVD process used here with KI5 copper precursor produced a consistent composition and deposition rate within the temperature range, 150-400°C (Figure 3.1) when deposited on planar ZnO. The initial thickness of the ZnO layer was measured at a minimum of 3 locations using an atomic force microscope (AFM) and an edge of the ZnO film patterned with a stainless steel scribe. After Cu_xS deposition, the combined Cu_xS/ZnO thickness was measured again with an AFM within 1mm of the previous scribes and the Cu_xS thickness was deduced from the difference.

Approximate stoichiometry measurements were performed with energy dispersive X-ray spectroscopy (EDS) and X-ray photoelectron spectroscopy (XPS). Table 3.1 illustrates the XPS energies used to calculate stoichiometry with the associated uncertainties. The Cu:S ratio was measured to be 1.8-2.1 at all deposition temperatures which is within the within the uncertainty of the EDS measurements due to the small amplitude of the sulfur peak . There are several different phases of Cu_xS with stoichiometry between x=1.8 to 2.1 and therefore EDS and XPS alone cannot be used to identify the chalcocite phase of the deposited film. Extended X-ray absorption fine structure (EXAFS) measurements described below are used to identify the specific phase of the
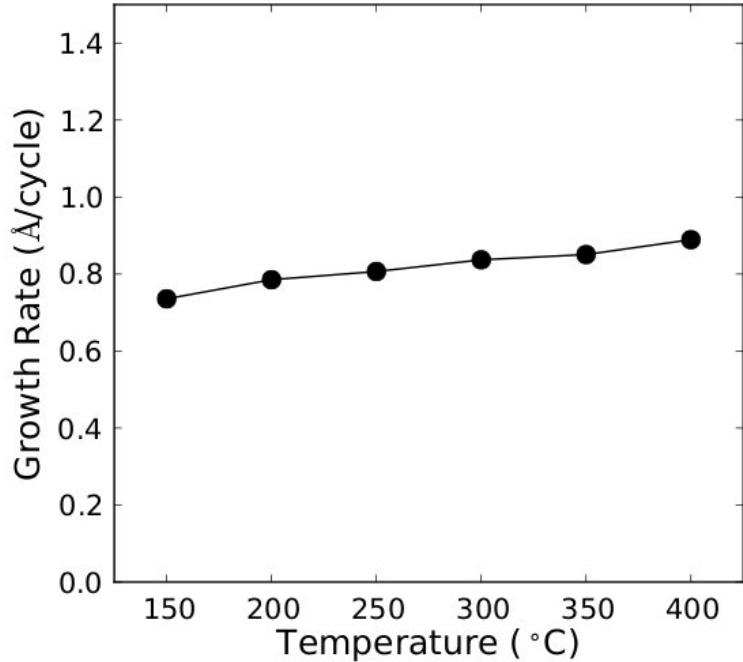
Figure 3.1: Growth rate and substrate temperature using alternating pulses of H_2S and precursor.

Cu_xS film. Nanoporous films of sintered 100nm TiO_2 nanoparticles were used to study the penetration of PCVD Cu_xS. Figure 3.2 shows cross-sectional SEM images taken of sintered nanoparticle TiO_2 films with and without PCVD treatment. The second film, with 900 cycles of PCVD Cu_xS deposited throughout, shows backfilling and a penetration depth of over 200nm. The PCVD deposited film appears to show uniform coverage

Peak Identity	Energy (eV)	Width (eV)	Area (eV)	Relative Concentration
Cu 2p	932	2.62	373	$67 +/- 2\%$
S 2p	162	2.75	12	$32 +/- 6\%$

Table 3.1: Typical XPS results used to determine composition for PCVD Cu_xS deposited at 400°C in a porous matrix of TiO_2.

throughout the TiO$_2$ layer.

a.   b.

Figure 3.2: Cleaved SEM cross section of a mesoporous TiO$_2$ film before (a) and after Cu$_2$S deposition (b). The porous TiO$_2$ film is successfully filled with PCVD Cu$_2$S.

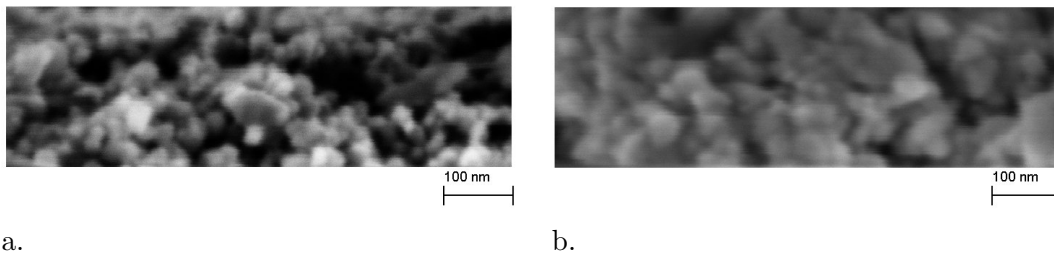The Cu K-edge EXAFS data were collected at the Stanford Synchrotron Radiation Light source (SSRL) on beamline 10-2, using a Si (111) double monochromator, detuned 50% to reduce harmonics. Slits with an approximate height of 0.5mm gave an energy resolution of 1.3eV. The data were collected in fluorescence mode (13-element Ge detector) at a temperature of 6K, with the X-ray polarization at either 10 or 80 relative to the film surface.

For these measurements, the Cu$_x$S film was deposited into a mesoporous TiO$_2$ substrate with 1000 cycles (approximate thickness if 80nm). The EXAFS data were reduced using standard techniques (RSXAP)[R1]. A Fourier Transform window of 3.511.0 -1 was used to transform the k-space data into r-space. The r-space plots show negligible variation between data collected for the two different polarization orientations, and in the rest of the analysis/discussion we only discuss fits for the 10 data set shown in Figure 3.3(c).

The purpose of the EXAFS measurements was to determine if the deposited PCVD films were Cu$_2$S, and not some other Cu$_x$S phase, as no diffraction peaks were
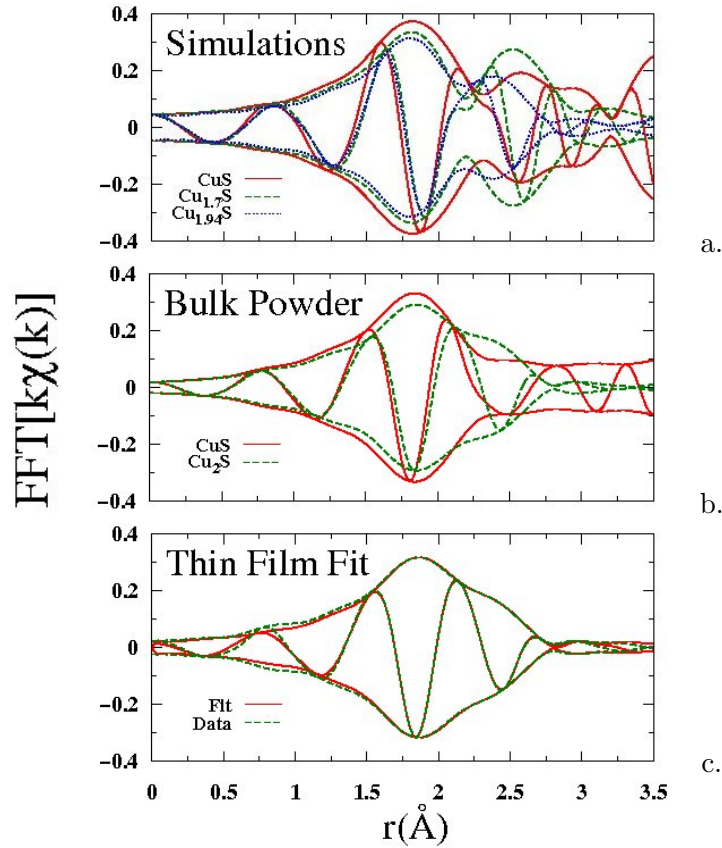
Figure 3.3: EXAFS r-space simulations for the CuS, $Cu_{1.7}S$, and $Cu_{1.94}S$ phases (a) showing a large variation in spectra for small changes in stoichiometry. (b) EXAFS r-space data for bulk CuS and Cu_2S. (c) Fits of the thin film data to a Cu_2S structure.

observable in the thin films formed inside the mesoporous TiO_2. EXAFS data for bulk CuS and Cu_2S were used in addition to the simulated data for several compounds, $Cu_{1.7}S$, $Cu_{1.94}S$ and CuS, to show how the r-space scans change with different amounts of copper present. The simulations were calculated using the known crystal structures, the FEFF8.2 code[R2], and a small overall broadening factor for the pair distribution functions, $ = 0.06$Å. In Figure 3.3(a) we compare the EXAFS r-space plots for these simulations, while in Figure 3.3(b) we compare the experimental data for the two bulk

51

samples. At 6K, Cu_2S has a large distinct shoulder between 2 and 2.5Åwhich corresponds to second neighbor copper atoms (Cu-Cu). As the fraction of copper decreases from 2 to 1.94 to 1.7, this shoulder moves away from the main Cu-S peak (nearest neighbor S) located near 1.8Åin the EXAFS plot. For $Cu_{1.7}S$ the shoulder becomes a well defined second peak near 2.55Å. In contrast, CuS has a significantly smaller shoulder (see Figure 3.3(b)). These plots show that the various Cu_xS phases can be easily differentiated.

Before fitting the PCVD film data, the bulk Cu_2S data was fit using two theoretical FEFF functions for Cu-S and Cu-Cu. The fit over the range 1.5-2.6Åwas excellent. The PCVD thin film data was then fit over the same r-range using the same FEFF functions as used to fit bulk Cu_2S. The excellent fit (solid line) is compared with the data (dashed line) in Figure 3.3(c). This result shows that the thin films deposited using PCVD are indeed Cu_2S films.

In addition to the EXAFS measurements, which look at the entire film thickness, XPS measurements were used to isolate the composition at the surface of the PCVD deposited Cu_xS films on TiO_2. The electron binding energies of the copper 2p and sulfur 2p electrons and relative concentration values (Table 3.1) are consistent with the Cu_2S phase of the material.[67]

3.3.2 CVD Results

To study resistance and optical absorption across a wide range of film thickness, CVD films were deposited on Corning glass. The CVD process was chosen over

the PCVD because a larger range of film thicknesses could be covered due to the higher film growth rate of CVD. Films over 100nm were not feasible for PCVD due to the long deposition times required and depletion of the H_2S source. CVD film could also be deposited directly on glass, which simplified the sheet resistance and optical absorption measurements. Films deposited via PCVD nucleated only on ZnO and porous TiO_2 and the presence of these under layers complicated absorption and sheet resistance measurements. It should be noted that EXAFS and energy-dispersive X-ray spectroscopy (EDS) measurements and EXAFS show no discernible compositional differences between CVD and PCVD films. Figure 3.4, shows four-point sheet resistance measurements of CVD-deposited Cu_2S films on glass plotted vs. film thickness. The sheet resistance is constant with thickness suggesting that a copper-poor material preferentially formed at the substrate/Cu_xS boundary, and effectively shorts out the Cu_2S film that forms the bulk of the film. The resistivity estimated from this sheet resistance is consistent with some previous studies on Cu_xS thin films, suggesting that x is in the range 1.9-2.019.[15, 66, 32] Other studies, however, report a widely varying range of resistivity values for the Cu_xS films, clouding the information required to isolate the specific material phase.[42, 20] PCVD films deposited in the porous TiO_2 matrix had sheet resistances that were too high to measure.

Conventional transmission spectroscopy had an insufficient dynamic range to resolve the low absorption tail and indirect band gap of the Cu_xS films. Instead, photothermal deflection spectroscopy (PDS) was used to measure optical absorption. The PDS technique requires the sample to be placed into contact with a material whose
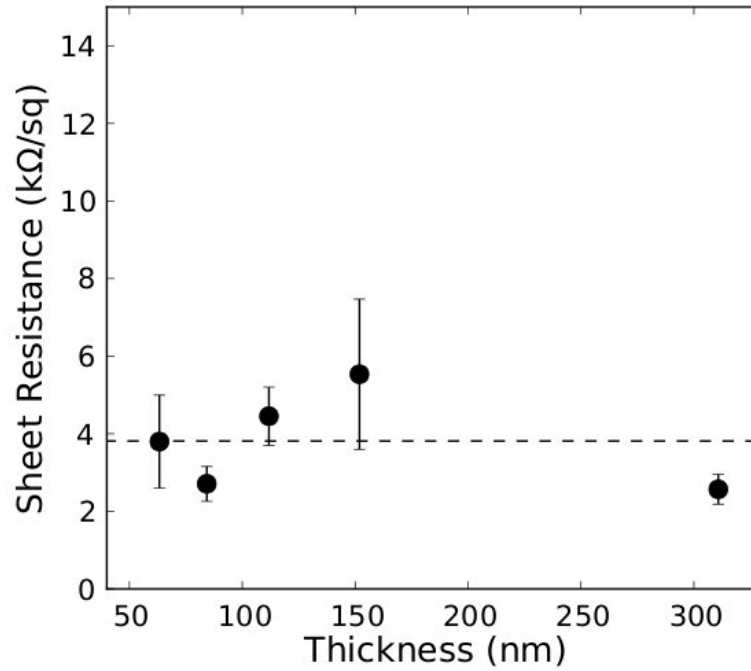
Figure 3.4: Sheet resistance and thickness for CVD deposited Cu$_x$S films showing the presence of a metallic layer at the Glass / Cu$_x$S interface.

index of refraction is sensitive to temperature. Absorption by the sample creates a temperature gradient in this surrounding material, and absorption measurements are achieved by measuring the deflection of a laser beam which is passed through the surrounding material. Figure 3.5 contains the absorption data for films with thicknesses ranging between 63.3-310.8nm deposited on Corning glass by CVD. Cu$_x$S films less than 100nm appear to show a high absorption in the infrared region due to free carriers. This behavior is consistent with more metallic copper-poor crystal phases.[32] Films greater than 100nm have distinguishable direct and indirect band gaps consistent with the copper-rich semiconducting crystal phases. Extrapolation of the the 310.8nm film absorption edges on the (hv)2 hv and (hv)1/2 hv plots revealed a direct band gap of

1.8eV and an indirect band gap of 1.2eV. Chalcocite is reported to have an indirect band gap in the range 1.05-1.21eV and a direct band gap of 1.7-1.8eV.[58, 56] The band gaps of copper-poor films are shifted higher than the Cu_2S values as the removal of copper ions results in the removal of electrons from the top of the valence band.[64] CuS and $Cu_{1.8}S$ have been reported to have an indirect band gap of 1.55eV while $Cu_{1.96}S$ has an indirect band gap of 1.4eV.[65] For x in the range 1.935-1.955, Cu_xS is reported to have a direct band gap of 1.3eV20. Previous studies have also shown band gaps between 1.85-2.16eV for x in 1.89-1.94.[20]
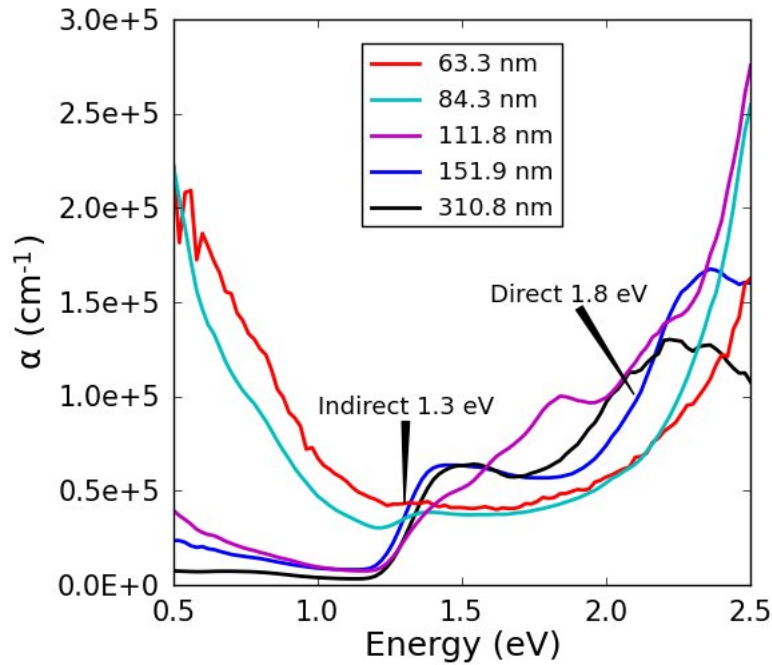

Figure 3.5: Optical absorption and thickness for a series of CVD deposited Cu_2S films showing metallic behavior for films less than 100nm thick and semiconducting Cu_2S for films greater than 100nm.

3.4 Summary/Conclusion

PCVD and CVD Cu_xS materials were deposited using the KI5 copper-organic precursor and H_2S gas. Consistent deposition rates in the temperature range 150-400°C and EXAFS analysis of the deposited films suggest that film composition is largely independent of substrate temperature during the deposition process. EXAFS was used to investigate the average compositional analysis of the PCVD Cu_xS films while XPS was used to study the surface layer of the deposited films. The majority of the film composition appear to be largely Cu_2S, but the planar resistivity measurements do not scale with film thickness and appear to be dominated by copper-poor states present in the film. Photothermal deflection spectroscopy was used to measure absorption at the surface of CVD Cu_xS deposited on glass. The results indicate copper-rich phases for greater thicknesses while thinner films appear show metallic copper-poor behavior. It is proposed that absorption in the thinner films is dominated by a copper-poor film region located near the substrate boundary whereas absorption for thicker films is dominated by copper-rich phase located closer to the surface.

3.4.1 Acknowledgments

Resources).

Chapter 4

Luminescent Downshifting Films for CdTe Cells

4.1 Introduction

4.1.1 CdS/CdTe

CdTe/CdS solar cells are among the most promising thin-film technologies. CdTe has an optimum band gap (1.5eV) and a high absorption coefficient of 105 in the visible range.[18] The CdTe/CdS junction shows a strong spectral response in the range 500-800nm,[37] and CdTe devices have achieved efficiencies of 16.5%.[96] CdTe devices are also proving to be cost competitive. The US company, First Solar, reports a CdTe module production cost of $0.75 per watt.

One mechanism for energy loss in CdTe/CdS devices results from CdS's high recombination rate and 2.41eV band gap.[59] Because the CdS layer is often placed

above the CdTe, light with wavelengths below 514nm is preferentially absorbed by the CdS and does not substantially contribute to the solar cell photocurrent.[59]

4.1.2 LDS Films

Researchers have tried reducing the thickness of the CdS layer and replacing the CdS window layer with wider band gap materials in order to reduce parasitic absorption. However, these methods inevitably alter the junction characteristics and the best known fabrication methods.[59] One approach that preserves the optimal cell characteristics and current fabrication processes is to place a luminescent down-shifting (LDS) material above the solar cell. The LDS film improves performance by absorbing short wavelength photons(<514nm) that would otherwise be absorbed by the CdS layer and emitting light at wavelengths(>514nm) that are more likely to be absorbed by the CdTe layer of the device.

In 1979, Hovel et. al. were the first to use plastic luminescent materials to improve the spectral response of solar cells.[38] In the past decade, a number of published works have focused on applying LDS materials to CdTe/CdS devices.[37, 59, 81, 60, 36] The most successful application of an LDS layer to improve CdTe device performance was achieved by Maruyama et al. using an organic dye suspended in PMMA.[60] PMMA is a well established luminescent host material with excellent optical properties and stability. PMMA has a lower absorption coefficient than low-iron, soda-lime or borosilicate glass in the visible[81] and has been shown to be stable in desert sunlight for over 17 years.[76] Long term stability is essential for materials used in solar

cell modules that will be functioning in exposed environments. PMMA also has a low monomer content and good solubilizing power.[80]

Stability problems that arise in organic luminescent materials are often caused by the photo-chemistry of luminescent dyes, which can degrade with exposure to illumination and air. One of the main sources of degradation occurs when the combination of UV light and oxygen or water photo-oxidizes the dye, causing it to fade. Other drawbacks of organic dyes include narrow absorption bands and relatively small Stokes shifts, which result in significant re-absorption losses.[48] Organic dyes provide an attractive option because they exhibit relatively high absorption coefficients, close to unity luminescence quantum efficiency (LQE), and are easy to process in polymeric matrices. This paper presents performance data and long time degradation data on luminescent films provided by Nitto Denko Inc. (Oceanside, CA). The films consist of PMMA doped with a proprietary organic luminescent dye, which will be referred to as Dye A in this article. Several dozen different dyes were evaluated, and Dye A was the most effective for CdTe device improvement. Dye A has proven to be stable for over 5000 hours at 50°C under one sun illumination.

This paper presents performance data and long time degradation data on luminescent films provided by Nitto Denko Inc. (Oceanside, CA). The films consist of PMMA doped with a proprietary organic luminescent dye, which will be referred to as Dye A in this article. Several dozen different dyes were evaluated, and Dye A was the most effective for CdTe device improvement. Dye A has proven to be stable for over 5000 hours at 50°Cs under one sun illumination.

4.2   Methods

4.2.1   Device Fabrication

The CdTe/CdS devices used to study the LDS film improvements were fabricated in the Beach Lab at the Colorado School of Mines. The process began with Pilkington TEC-7, a commercially available encapsulation glass coated with SnO_2 to serve as a front contact. A window layer of CdS was evaporated onto the SnO_2 and CdTe was deposited on the CdS layer by a physical vapor deposition process. The CdTe layer was treated with $CdCl_2$ and annealed to recrystallize the CdTe layer and increase mobility. After a short bromine etch, the back contact was deposited by evaporating a layer of ZnTe and Cu followed by a layer of Au. The CdTe devices were characterized independently as well as with LDS films attached to the glass encapsulation. LDS films were attached using Saint Gobain BC600 optical coupling grease. The device structure can be seen in Figure 4.1. The device fabrication process allows for the formation of multiple devices on a single TEC-7 slide. A custom mask was used to isolate individual devices and to prevent optical coupling of the LDS film and excess optical coupling grease to the light source.

The LDS films in this study were 20-100$_m u$m thick and consisted of host PMMA doped with organic luminescent dyes. When light enters a luminescent film, it can be absorbed by the luminescent dye and re-emitted at a lower energy due to a Stokes shift. Light emitted by the luminescent material can be emitted in any direction. As a result, down-shifted light may be lost back through the surface of the LDS mate-
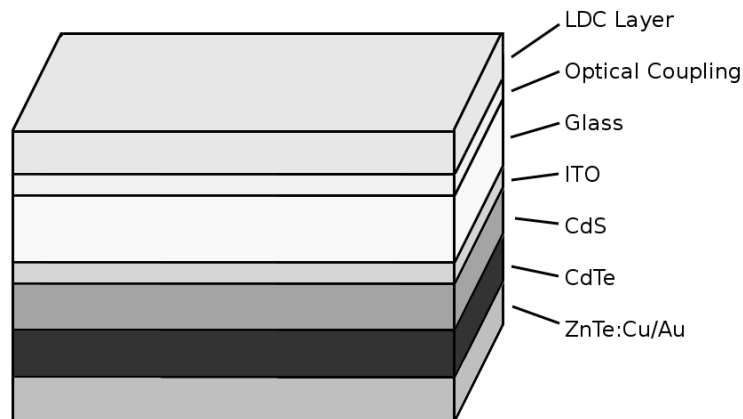
Figure 4.1: Stack including CdTe/CdS device and LDS layer.

rial, internally reflected by the air/LDS boundary, re-absorbed by the LDS material, or passed down into the solar cell as desired.

4.2.2 Measurements

The CdTe devices were electrically characterized with and without LDS films attached to the glass encapsulation layer. Typically, the measurements were repeated 3-10 times / film to confirm reproducibility. The illumination was provided by 5 tungsten halogen lamps providing 100 mW/cm^2 intensity. IV curves were taken with a source-measure unit using a voltage step of 50mV, and a hold time of 40ms.

To test the intrinsic stability of these dyes, the LDS films were sealed in an all-metal seal container in a nitrogen glove box to prevent exposure to air or water during a light soaking test. The glass seal used optical grade corning 7056 glass with a UV

cutoff at 300nm. These sealed containers were then placed under a metal-halide lamp with a high UVA component and calibrated to 1000 W/m2. Liquid cooling maintained the temperature at at 50°C during the long time degradation tests. The glass windows permitted the periodic measurement of optical transmission without breaking the seal.

4.3   Results

4.3.1   Performance

The absorption edge of CdS with band gap of 2.41eV is 514nm.[59] An effective LDS film would absorb light below 514nm and emit light above 514nm to reduce parasitic light absorption by the CdS layer in a CdTe/CdS device. An ideal LDS would have a high luminescent quantum efficiency (LQE) and an emission spectrum that is well matched to the external quantum efficiency (EQE) of the CdTe/CdS solar cell (which can be seen in Figure 4.5). The emission spectrum of Dye A is shown in Figure 4.2.

The dye concentration in PMMA was varied between 0.05-2 wt.% and film thicknesses was varied between 20-100m. The efficiency improvement of the CdTe/CdS devices was found to be a strong function of dye concentration. As dye concentration increased, LQE dropped due to increased quenching and self absorption losses. This trend can be seen in the relative improvements shown in Figure 4.3.

When both concentration and thickness of LDS film were optimized, an 8.5% improvement was observed in short circuit current and efficiency for a CdTe/CdS solar cell as shown in Figure 4.4.
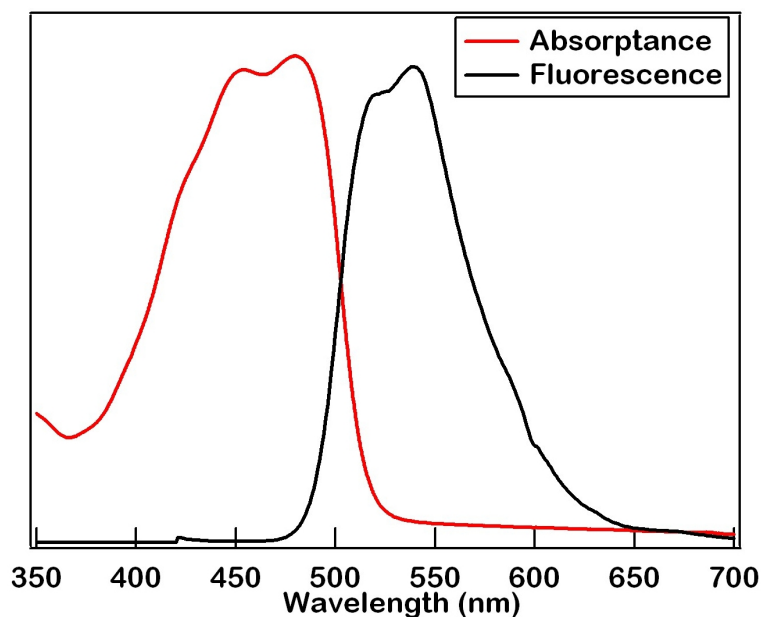
Figure 4.2: Emission spectrum of LDS film for absorption of photons below 514nm and emission above 514nm.

The improvement in short circuit current and efficiency was also reflected in the external quantum efficiency measurements presented in Figure 4.5. The efficiency for a CdTe/CdS device at wavelengths less than 514nm is very low due to the absorption in the CdS window layer. An attached LDS film increases the effective quantum efficiency in this region because photons that would normally be lost to absorption in the CdS layer are converted to longer wavelengths and collected by the CdTe layer.

4.3.2 Reliability

The dominate degradation mechanism for organic dyes is photo-induced oxidation. High energy photons can break chemical bonds in the organic dye, but bonds

64
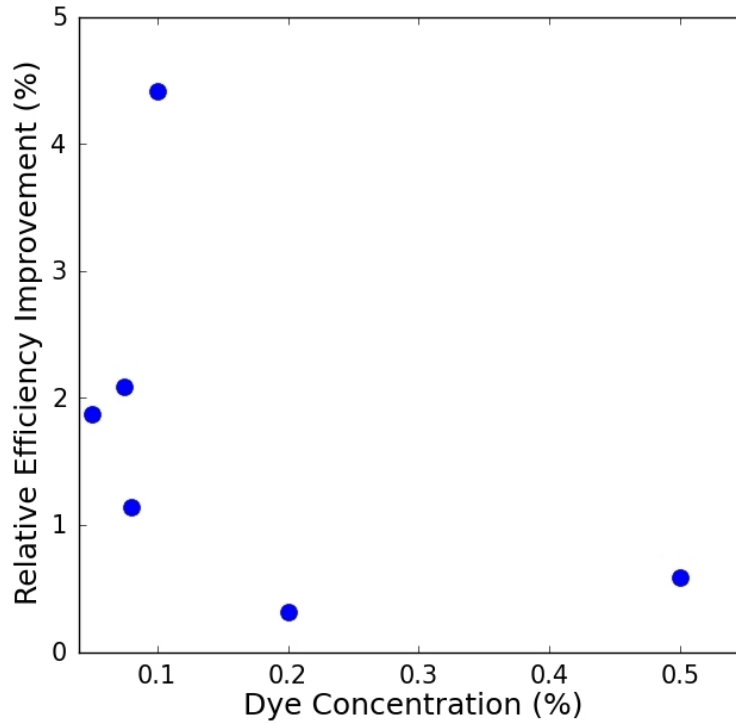
Figure 4.3: Relative efficiency improvement vs dye concentration. The efficiency gain drops due to quenching and self absorption.

can often reform unless there is another chemical species present to irreversibly react with the broken bonds. Oxygen radicals and OH species are the most common chemical reactant for photo induced degradation because organic materials have a high propensity to absorb oxygen and water from the atmosphere. Isolating the organic materials from water and oxygen during light soaking tests is essential to separate the intrinsic photo-stability of the dye from the photo induced oxidation of the dye. The purpose of these stability studies is to establish the intrinsic long term stability of the LDS film assuming that it has perfect encapsulation. Most current thin film photovoltaic modules are hermetically sealed to withstand corrosive under adverse outdoor environmental

65
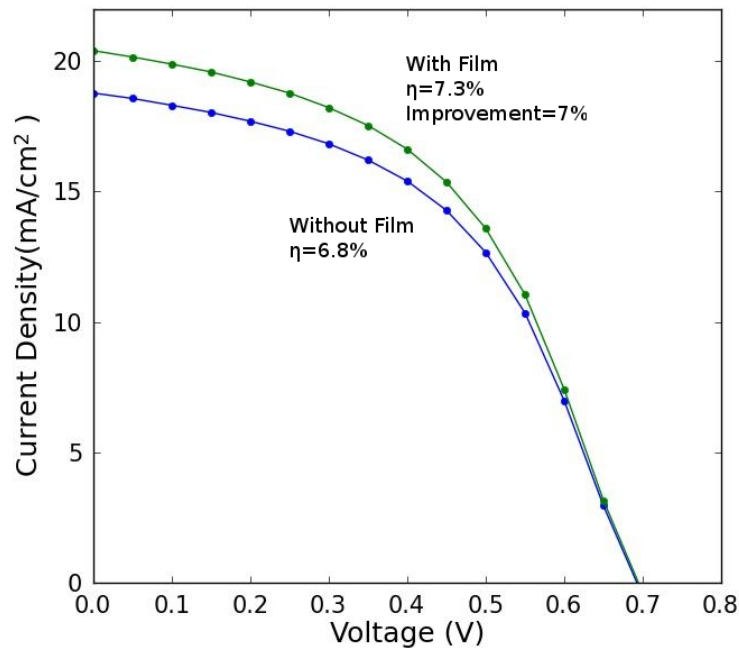
Figure 4.4: Current voltage curves for a CdTe/CdS cell with and without an LDS film.

conditions.

An encapsulation vessel was developed to establish the intrinsic reliability of an organic dye for up to 10,000 hours. The encapsulation vessel used all metal-metal and metal-glass seals to prevent the diffusion of water and oxygen that can occur with polymer seals. Technical grade, fused silica windows permitted optical measurements to be performed during the long time tests without breaking the seal. The LDS film samples were sealed in the encapsulation vessel in a nitrogen glove box with <1 ppm of oxygen and water. Figure 4.6 shows an example of an all metal seal container with 4 dye samples after 500 hours of exposure at one sun and 50°C. As a colored dye degrades it becomes more transparent. Three of the LDS films in Figure 4.6 have lost their green
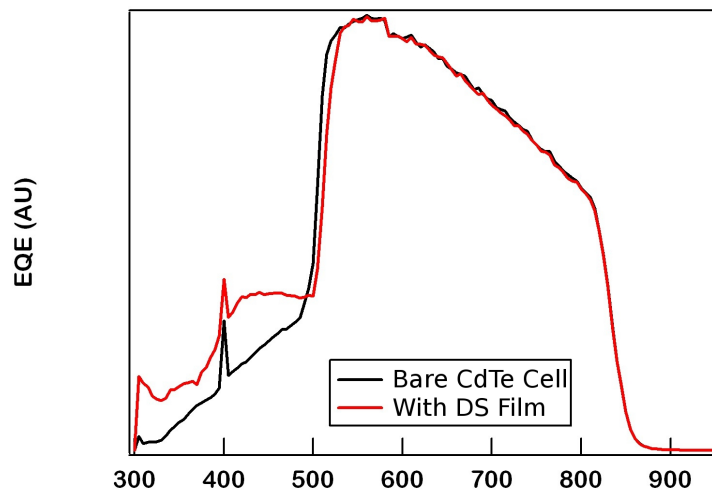
Figure 4.5: External quantum efficiency of device with and without LDS film. The plot shows improved current between 300 and 500nm due to the down-shifting of photons in this range to a lower energy.

color due to degradation. One LDS film remained unchanged after 500 hours at one sun.

The effects of air and illumination are shown more quantitatively in Figures 4.7 and 4.8. Figure 4.7 presents the absorption spectrum of Dye A when exposed to 750 hours of illumination in air while Figure 4.8 shows the absorption of Dye A while encapsulated in dry nitrogen. Only when the dye is encapsulated is it stable under long term light exposure.

These stability tests have been continuing on a select set of dyes for 5000 hours at one sun of illumination and 50°C. Figure 4.9 shows the peak absorption at 475nm as a function of time for the same dye shown in Figures 4.7 and 4.8. No detectable change in peak absorption has been observed for two LDS films encapsulated in nitrogen for
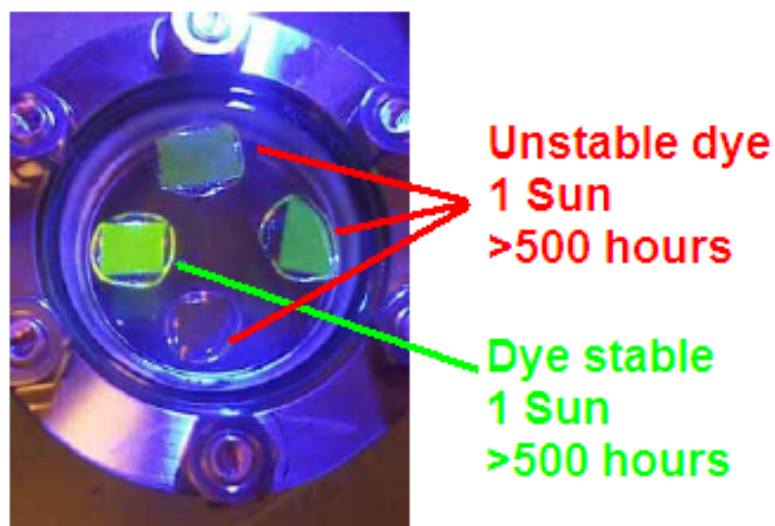
Figure 4.6: Example of metal seal encapsulation cell used to test the intrinsic stability of LDS films under illumination. All dyes except the green dye on the left showed signs of degradation after 500 hours of testing.

>5000 hours.

4.4 Conclusion

An organic luminescent down-shifting film has been demonstrated that can provide up to a 8.5% improvement in efficiency for a CdTe/CdS solar cell. This film is stable for at least 5000 hours under one sun illumination provided that the film is protected from oxygen and water. Conventional CIGS solar cells must also be encapsulated for long term reliability and may be compatible with these organic dyes.
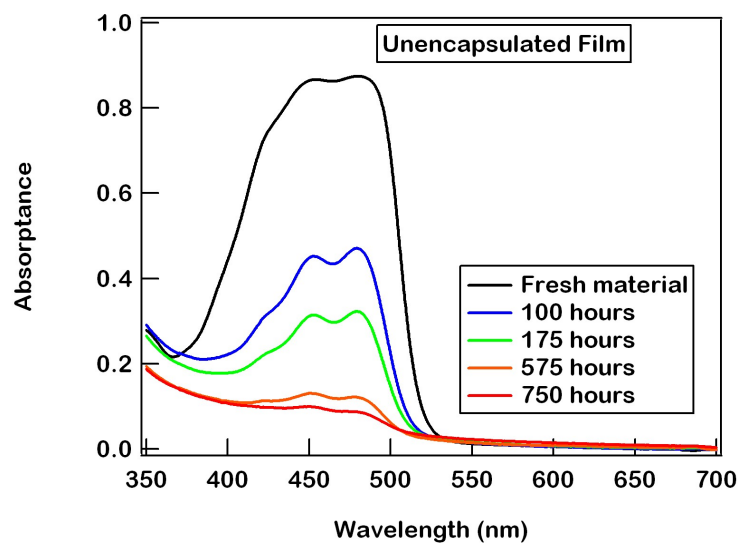
Figure 4.7: Absorption spectrum evolution during 750 hours of exposure at one sun illumination in air.

4.4.1 Acknowledgements
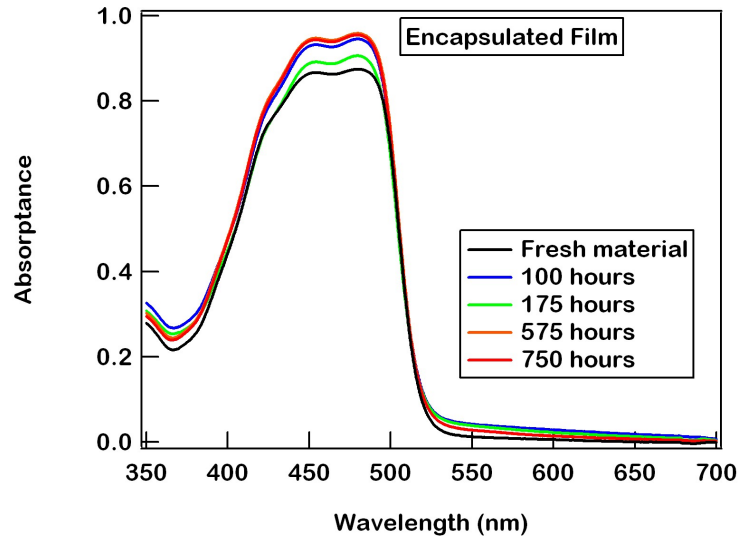
Figure 4.8: Absorption spectrum evolution during 750 hours of exposure at one sun illumination in dry nitrogen.
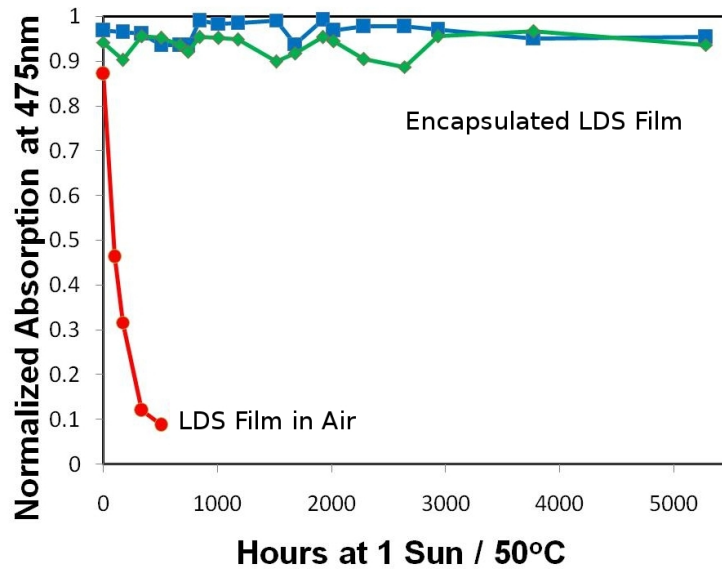
Figure 4.9: Absorption at 475nm after long term exposure to one sun illumination in air and dry nitrogen. The LDS films are stable provided that they are encapsulated.

70

Chapter 5

Modeling of Transport in Nanocrystalline PbSe Films

5.1 Introduction

5.1.1 PbSe Nanocrystals

Inorganic semiconductor nanocrystals, or nanoparticles, have been developed for use in a number of applications including field effect transistors (FETs), photodetectors, and solar cells.[54] The optical, electrical, and magnetic properties of nanocrystals depend strongly on the crystal size.[90] They therefore represent a new class of cheap and easily-processable materials whose physical properties can be tailored to a specific application.

Nanocrystalline PbSe is particularly well-suited for solar cell applications due to its band gap, which is size-tunable across most of the solar spectrum (0.5eV and

above).[45, 94, 7] It also exhibits hot electron transport properties,[88] high carrier mobilities,[54, 46, 87] ambipolar charge transport,[54, 46, 87] and efficient carrier-multiplication (CM).[84, 75, 26, 25] Motivated by theoretical efficiencies of up to 42%,[49] researchers have launched numerous efforts focused on developing PbSe nanocrystal solar cells.

One area of recent interest concerns the dependence of electron and hole mobilities on the average nanocrystal size in PbSe systems. Two groups carried out transport measurements of films composed of by PbSe nanocrystals linked by ethane dithiol ligands. Both groups reported a sharp rise in mobilities/conductivities in the 3-5nm crystal diameter range followed by a sloping decay in the $6 - 8$nm range.

This paper describes efforts to develop and identify a class of models that can account for these observed trends. We report a Monte Carlo model for charge transport in an array of nanocrystals that uses PbSe material-specific parameters and incorporates carrier interactions and disorder effects. Simulations agree with experimental mobilities/conductivities and explain both the sharp rise and the sloping decay.

5.1.2   Field Effect Measurements

Field effect mobility measurements by Liu et al. and conductivity measurements by Kang et al. revealed interesting trends in nanocrystalline PbSe films.[54, 46] In both studies, electron transport increased by roughly an order of magnitude when the nanocrystal diameter, d_{crystal}, increased in the range, 3-5nm.[54, 46] Both groups also observed a mobility/conductivity peak between $d_{\mathrm{crystal}} = 5 - 6$nm followed by a sloping decay. While this sloping decay extends out to 9nm in the data collected by Liu

et al., Kang et al. observed a local minimum around 7nm with a maximum conductivity occurring around 9nm.[54, 46] In addition to electron transport, Liu et al. also measured hole mobilities, which increased with nanocrystal size by just under two orders of magnitude in the 3-5nm range.[54] This paper reports our efforts to understand the steep rise in mobilities/conductivities in the 3-5nm diameter range as well as the saturation and sloping decline of mobilities at larger crystal sizes.

5.1.3 Modeling-Overview

There has been one reported work regarding these mobility/conductivity profiles. In 2012, Lee and collaborators simulated transport in PbSe films using five connected quantum wells in a tight binding system bath model.[51] Though their theoretical framework was able to capture and track quantum-coherent processes, they found that the dominant transport mechanism was incoherent hopping between nearest neighbor sites. While the calculated mobilities displayed the experimentally observed rise in the $d_{crystal} = 3 - 5$nm region, the magnitude of the rise was considerably lower than the observed one.[51] One notes that such small scale tight binding calculations have difficulties capturing disorder effects. Further, the description of the treatment of the charging processes and temperature effects left open questions as well.

To capture charging and disorder effects more effectively, we have developed a Monte Carlo approach. Our simulations are able to reproduce the PbSe nanocrystal film behavior accurately by incorporating (1) site disorder, and (2) occupancy-dependent charging energies for multiply-occupied nanocrystals. Our model assumed a constant

inter-crystal spacing equal to the nanocrystal capping ligand length and can easily be applied to a wide variety of film geometries and FET and solar cell device structures.

5.2 The Hopping Model

Our model is motivated by the temperature-dependent measurements of Kang, which suggest that transport in PbSe films is dominated by a nearest neighbor hopping mechanism at room temperature.[46] Our numerical approach, developed from the Miller-Abrahams framework [62] by Bassler and others, has been used extensively to study charge generation, transport, and recombination in disordered organic devices.[14, 57, 98, 97, 93] Here, we adapt the hopping model to our inorganic system. The nanocrystalline PbSe film is represented as a regular cubic lattice. Each lattice site corresponds to an individual nanocrystal, and charge transport is represented as a directed random walk of excited carriers drifting between PbSe nanocrystals. The dominant transport channel is that of incoherent thermally activated tunneling between nearest neighbor sites/crystals. Hopping rates are determined by site energies and the overlap of wave functions between neighboring nanocrystals. 5.1 illustrates the considered transport mechanism.

Each lattice site in the Monte Carlo model is characterized by two parameters: an occupation number, indicating the number of carriers located at that site, and the site energy, which equals the lowest unoccupied molecular orbital (LUMO) or the highest occupied molecular orbital (HOMO) level of the host nanocrystal for electron and hole

74
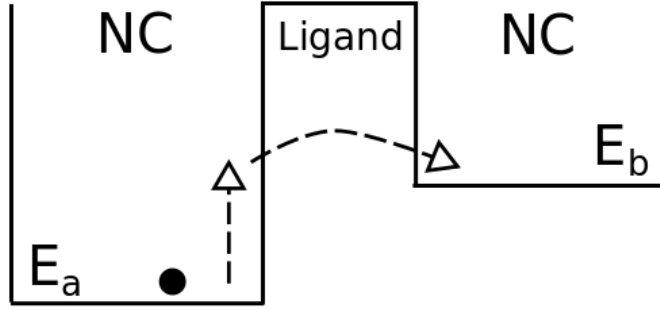
Figure 5.1: Diagram of studied transport mechanism. In this hopping model, transport occurs via thermally activated tunneling across the ligand barrier. Crystals in the lattice have an localized electronic structure, which depends on crystal size.

conduction, respectively.

At the beginning of the simulation, lattice sites are populated at random by an ensemble of carriers until a predetermined carrier density has been achieved. The carrier density is chosen to be consistent with experimental values. Each carrier is then assigned a residence time, t_a, representing the time elapsed before the carrier moves from its current site to a neighboring site. Following the work of Nelson and Chandler,[17] residence times are calculated by

$$t_a = \frac{-\ln(r)}{\sum\limits_{i=1}^{N_{\text{neighbors}}} \Gamma_{a \to i}}, \quad 0 \leq r < 1, \tag{5.1}$$

where $N_{\text{neighbors}}$ is the number of nearest neighbors, r is a random number less than one, and $\Gamma_{a \to i}$ is the hopping rate calculated for a transition between the initial site (a), and a neighboring site (i). A Miller-Abrahams expression,[62]

$$\Gamma_{a \to b} = \alpha\beta \begin{cases} \exp(\frac{E_a - E_b - ql\mathbf{F_z}\cdot\hat{\mathbf{u}}_{\mathbf{ab}}}{k_B T}) & \text{if } E_a - E_b - ql\mathbf{F_z}\cdot\hat{\mathbf{u}}_{\mathbf{ab}} < 0 \\ 1 & \text{if } E_a - E_b - ql\mathbf{F_z}\cdot\hat{\mathbf{u}}_{\mathbf{ab}} \geq 0 \end{cases}, \qquad (5.2)$$

is used to calculate the hopping rate for a transition from the initial site, a, to destination

site, b. Here, α is a dimensionless prefactor used to scale the maximum hopping rate,

β is the tunneling amplitude determined by the wave function overlap of neighboring

nanocrystals, E_a and E_b are the energies of the initial and destination sites, respectively,

and q is the elementary charge. $\mathbf{F_z}$ is the external field, $\hat{\mathbf{u}}_{\mathbf{ab}}$ is a unit vector along the

hopping direction, k_B is the Boltzmann constant, and T is the temperature of the

system. l is the hopping distance, equal to $d_{\text{crystal}} + d_{\text{ligand}}$, which are the nanocrystal

diameter and the ligand length, respectively.

The residence times assigned to each carrier are listed in a time queue, which

is used to determine all future actions. Before each hopping event, the carrier with the

shortest residence time is selected from the time queue. Next, a destination location is

determined following the example of Nelson and Chandler.[17] If we define γ_b as

$$\gamma_b = \sum_{i=1}^{b} \Gamma_{a \to i} \bigg/ \sum_{i=1}^{N_{\text{neighbors}}} \Gamma_{a \to i}, \quad \text{for } b \in (1 \dots N_{\text{neighbors}}) \qquad (5.3)$$

then the probability of selecting a particular destination site b is defined as,

$$P_b = \gamma_b - \gamma_{b-1} \qquad (5.4)$$

.

A particular destination site b is selected if a random number, r, satisfies $\gamma_{b-1} \leq r \leq \gamma_b$ for $0 < r < 1$. After each hop, the total simulation time is increased by the hopping carrier's residence time, and the residence times of future events listed in the time queue are reduced accordingly. A new residence time is then stored for the hopping carrier at its new location.

In a simulation lattice of spatial dimensions, X×Y×Z, the source and drain electrodes are represented by the z=0 and z=Z+1 planes, respectively. When a carrier transitions from z=Z-1 to z=Z, it is immediately harvested by the drain electrode, the total number of harvested carriers is updated and recorded, and the carrier is re-injected at a randomly selected site on the z=1 plane. Throughout the simulation, an external electric field is applied in the $\hat{z}$ direction. Periodic boundary conditions are used for carrier motion in the $\hat{x}$ and $\hat{y}$ directions. Simulation results presented in this letter use a lattice size of X=Y=5 and Z=200 sites. These dimensions represent a region in which simulation results are stable and independent of lattice size. More information regarding finite size effects and model testing are provided in the supplementary material.

Simulations are divided into measurement intervals, which are defined by the time required for 10000 carriers to be harvested through the z=Z+1 electrode. At the end of a measurement interval, the total current, J, is given by the total charge harvested at the drain electrode divided by the total simulation time. J, in turn, allows for an easy mobility calculation.

$$\mu = J/q\rho F_z, \tag{5.5}$$

77

,

where ρ is the carrier density. After calculating the mobility at the conclusion of the measurement interval, a new measurement interval is initiated by continuing the simulation in its current configuration. At the conclusion of the next measurement interval, the mobility is calculated and compared to the value from the previous interval. When the successive mobilities are within a tolerance of 1%, the latter mobility is recorded and the simulation is terminated. This method ensures that the simulations reach a steady state.

5.2.1 Tunneling

The β term in Equation 5.2 represents the wave function overlap of neighboring nanocrystals and determines the amplitude of the tunneling process. To calculate β, we first solve for energy splittings following the method outlined by Lee and Brennan.[11, 51] In this method, a two-nanocrystal system is approximated by two quantum wells defined by three potential barriers. A transfer matrix solution determines the transmittance T as a function of carrier energy. Generally, T exhibits two maxima separated by an energy splitting, and β is approximated by one-half of the energy splitting divided by Planck's constant. 5.2 shows the calculated energy splittings as a function of nanocrystal diameter.
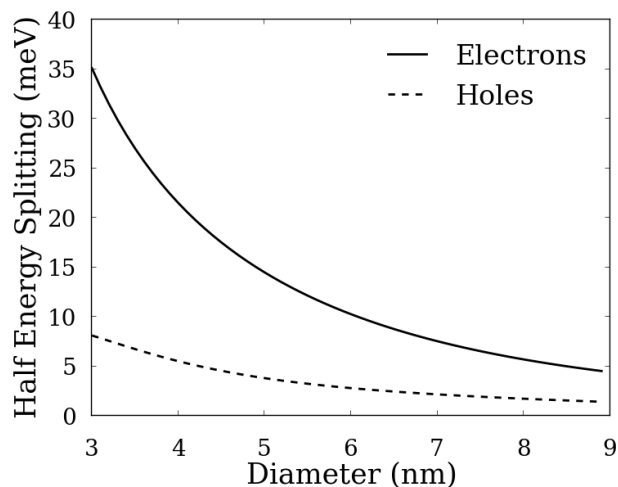
Figure 5.2: One half of the energy level splitting in the first excited states of the double quantum well. Electron energy splittings exhibit a significantly stronger dependence on nanocrystal size than holes.

5.2.2 Site Energies

E_a and E_b in Equation 5.2 are determined by the nanocrystal sizes assigned to each location in the simulation lattice. For the simulation of films of mean crystal size, d_{crystal}, we distribute the crystal sizes according to a Gaussian distribution of mean, d_{crystal} and standard deviation, $\sigma(d_{\text{crystal}})$. Colloidal nanocrystal size generally becomes more difficult to control as crystal size increases.[54, 46, 23] This is captured by using a standard deviation that increases with diameter:

$$\sigma(d_{\text{crystal}}) = \sigma_0 d_{\text{crystal}}, \tag{5.6}$$

where σ_0 is a parameter constant across all crystal sizes.

The site energies, given by the LUMO energy levels for electron carriers, and

79
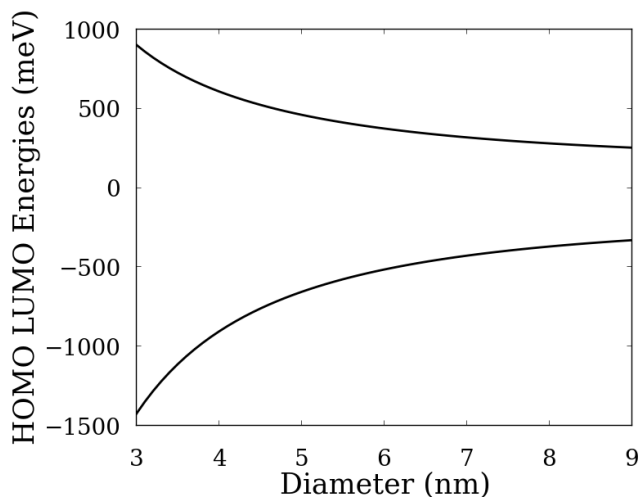
Figure 5.3: HOMO and LUMO energies for NC PbSe used in hopping simulations. Values were calculated by Kang and Wise[45].

the HOMO levels for hole carriers, were calculated by Kang and Wise for a range of nanocrystal diameters.[45] We assign site energies to each site by adopting the Kang-Wise values corresponding to their designated sizes. 5.3 shows the HOMO and LUMO levels used in our simulation.

5.2.3 Charging Energies

When a lattice site is occupied by a second carrier, the total energy used to calculate residence times is increased by a charging energy $E_c(d_{\text{crystal}})$:

$$E_C(d_{\text{crystal}}) = X_C/d_{\text{crystal}}, \tag{5.7}$$

where X_C is a charging parameter incorporating the effect of the dielectric environment. In agreement with previous work, adding the N-th carrier to a single nanocrystal re-

quires a charging energy of $(N - 1)E_C$.[6] To be more precise, when a carrier is hopping

off a site a, the hopping rate is calculated by using the charging energy,

$$E_a = E_{a_0} + (N_a - 1)E_C(d_{\text{crystal}}).\tag{5.8}$$

where E_{a_0} is the unoccupied HOMO/LUMO value taken from 5.3. If a carrier is hopping

to a destination site, b, with N_b carriers already on it, then the charging energy used in

the hopping rate calculations is given by

$$E_b = E_{b_0} + N_b E_C(d_{\text{crystal}}),\tag{5.9}$$

,

with E_{b_0} taken from 5.3.

It is worth noting that the HOMO and LUMO energy levels in PbSe are four-fold degenerate by spatial symmetry and two-fold degenerate by spin.[45, 6]. Therefore, we allow a maximum of eight carriers to occupy each lattice crystal/site. At the simulated densities, it is extremely rare for a site to be occupied by more than five carriers.

5.3   Tests of The Model

The first test presented in this appendix evaluates simulation results in a situation where an analytical solution exists. Following Nelson and Cass, [68, 16] we assign residence times drawn from a Poisson distribution,
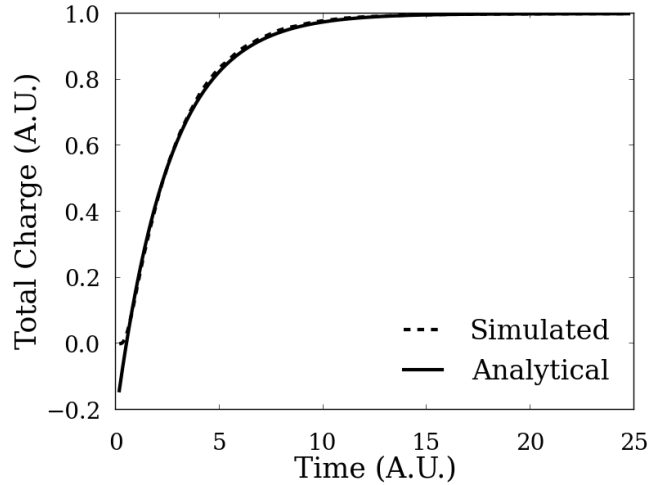
Figure 5.4: Harvested charge vs. simulation time using residence times drawn from the Poisson distribution. Results are compared the diffusion equation solution.

$$\psi(t) = 1/\tau \exp(-t/\tau), \tag{5.10}$$

.

Under these conditions, simulations will be statistically identical to a simple random walk with time step, τ.[68] Flight directions are then chosen with all six neighbors weighted equally. Simulations are carried out by injecting carriers into the z=1 plane at t=0 and recording the total charge extracted from the z=Z+1 plane as a function on time. Results consistent with a random walk of time step, τ, should match the solution to the diffusion equation with diffusion constant, $D = l^2/6\tau$. Here, l represents the hopping distance. 5.4 shows that the simulated and the analytical results are consistent.

In a second set of tests, mobilities are calculated while varying the simulation lattice dimensions to characterize finite size effects. Measurements are made each time

82
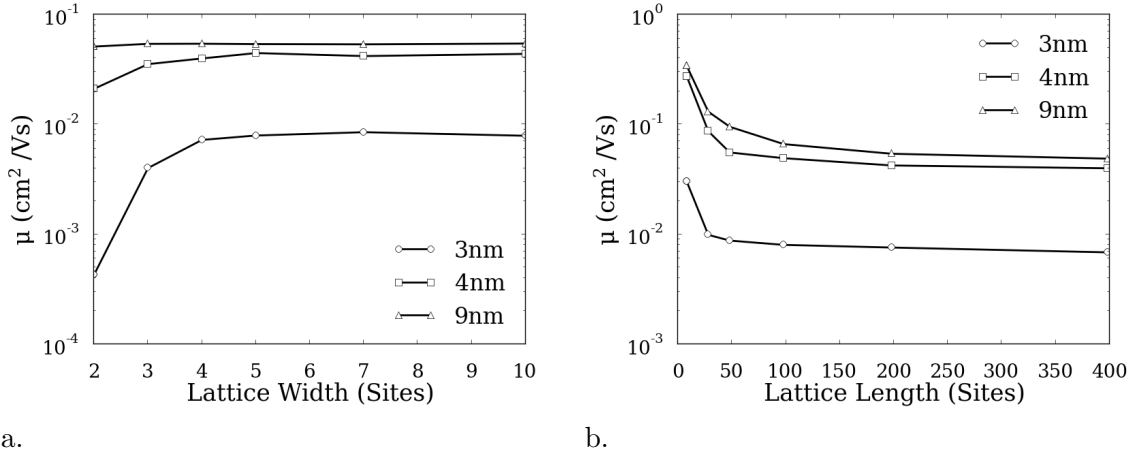
Figure 5.5: Finite size effects in the direction perpendicular to the external electric field (a) and along the external field (b). Results presented in this study used lattice dimensions of X=Y=5 and Z=200 sites.

10000 carriers are collected. Values are recorded and the simulation is terminated when successive iterations yield measurements within 1% of each other. In 5.5a, the X and Y lattice dimensions are varied while holding the Z dimension constant at 200 sites. Simulations with X and Y dimensions equal to or greater than 5 represent a stable region. In 5.5b, the X and Y dimensions are held equal to 5 while the Z dimension is varied. Results suggests that the behavior is stable when the Z dimension is greater than 100 sites. For results presented in the sections above, lattice dimensions were set at X=5, Y=5, and Z=200 sites.

5.4   Results

In 5.6, we present the results of our simulations alongside the electron and hole mobilities measured by Liu et al.[54] and electron conductivities measured by Kang et
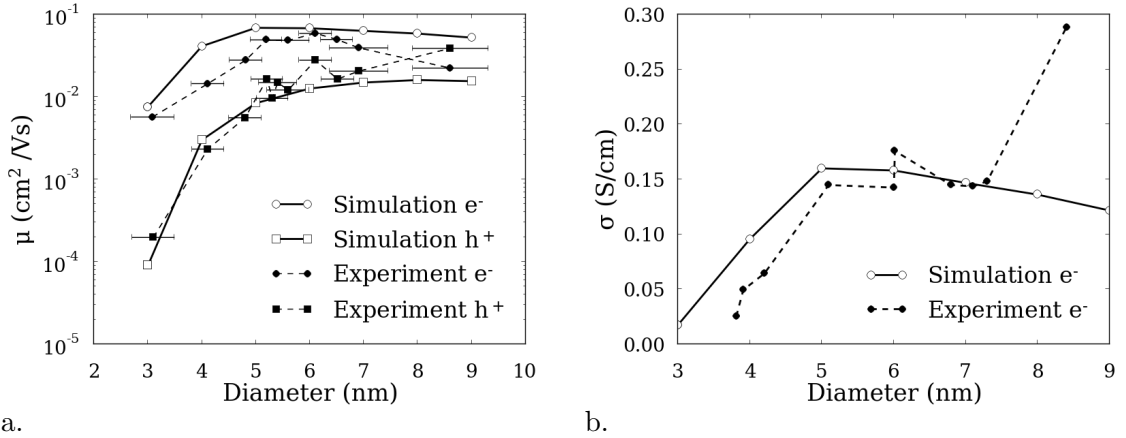
Figure 5.6: Simulated electron and hole mobilities, produced by the hopping model, plotted with experimental data published by (a) Liu et al. [54], and electron conductivities published by (b) Kang et al.. [46]

al.[46] It is recalled here that the conductivity is defined as the product of the carrier mobility and the carrier density.

The results will be discussed in two parts by distinguishing the low diameter region ($d_{\mathrm{crystal}} = 3 - 5\mathrm{nm}$) and the large diameter region ($d_{\mathrm{crystal}} = 6 - 9\mathrm{nm}$) of 5.6. For crystal diameters in the $3-5\mathrm{nm}$ range, the electron mobility/conductivity increases by roughly an order of magnitude with increasing nanocrystal size. Hole mobilities in this region increase by roughly two orders of magnitude. There are two main factors explaining these steep increases. (1) As the average crystal diameter increases, hopping distances increase. It follows that a decreasing number of hops are necessary to traverse a given film length, and mobilities/conductivities increase as a result. (2) The presence of site energy disorder generates larger barriers to hopping at smaller nanocrystal diameters. Referring back to 5.3, we see that the HOMO and LUMO energy levels of individual nanocrystals have a stronger dependence on nanocrystal size at smaller diam-

84
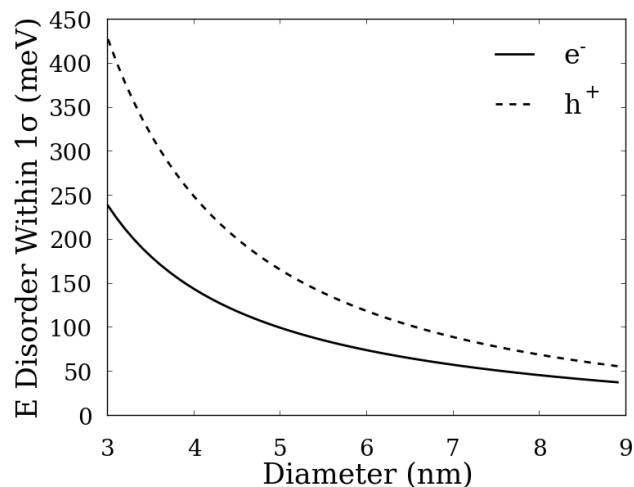
Figure 5.7: Energy variation within one σ of the LUMO (solid) and HOMO (dashed) levels. Crystal sizes have a normal distribution, and site energies are determined according to 5.3.

eters. Therefore, the appropriate size disorder, given by Equation 5.6, induces greater site energy disorder for smaller nanocrystals. Greater site energy disorder results in larger barriers in the Miller-Abrahams hopping rate, leading to longer residence times and lower mobilities for smaller crystal sizes.

5.7 illustrates the size dependence of the site energy disorder in our simulations. Here, crystal sizes are distributed with a standard deviation of 9% of the average crystal diameter. The vertical axis shows the range of site energies within one σ around the mean. Site energies are distributed over a much wider range at smaller crystal diameters. One observes that holes site energies are significantly more sensitive to size disorder than electron energies, and hole mobilities exhibit a more dramatic increase in the 3-5nm range.

To summarize, the increasing distances covered by each hop and the decreasing

site disorder are the two key factors, driving the sharp increase of the mobilities at low crystal sizes.

5.6 shows that at larger diameters, the sharp rise of the electron mobilities give way to a sloping downward trend in the data of Liu et al., and to a plateau region in the data of Kang et al..[54, 46] While the hole mobilities continue to rise, this rise is dramatically lower than in the small-diameter regime. In the $d_{\text{crystal}} > 6$nm region, the simulated mobilities also show a sloping downward trend with increasing nanocrystal size. There are two major factors, explaining this sloping behavior. (1) The wave function overlap and therefore the β tunneling amplitude decreases with increasing diameter due to lower ground states with respect to the ligand barrier height. (2) Transport is also penalized at larger crystal sizes due to more frequent carrier interactions.

A more detailed explanation of (2) is that the number of carriers per site is greater in systems with larger crystals, assuming a constant carrier density. With increasing crystal size, carriers more frequently encounter sites of higher occupation. Since the energy of a destination site is greater when the site is already occupied, the residency time of the hopping carrier is increased. This inhibits transport. 5.8 demonstrates this effect. The right vertical axis shows how the carrier/site density increases with increasing crystal diameter for the fixed carrier density of 0.002 carriers/nm^3. This value was chosen to be relevant for the experiments of Liu et al. and Kang et al. The left vertical axis shows the average charging penalty incurred per hop, which increases rapidly as the average site occupation approaches one. These plots provide clear evidence that transport occurs through pathways that involve a rapidly increasing number

86
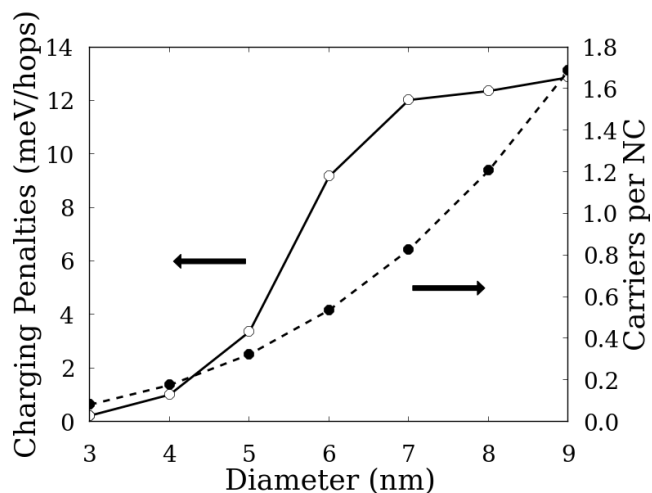
Figure 5.8: The average charging energy barrier per hop (open circles) and the number of carriers per nanocrystal at 0.002 carriers/nm^3 (closed circles). At smaller crystal sizes, multiple carriers are less likely to occupy a single nanocrystal.

of multiply occupied sites, resulting in increasing charging energy costs.

It is noted that there are two competing factors related to charging energy. On one hand, the actual charging energy parameter E_c decreases with increasing crystal diameter. This led Lee et al. to conclude that diameter dependence of the charging energy is responsible for the rapid rise of the mobility in the small diameter region.[51] On the other hand, the charging energy cost is only incurred only if carriers interact during transport. Our 5.8 implies that for small nanocrystal sizes, multiple carriers are not forced to occupy the same nanocrystal, thus the charging processes have negligible impact on transport. We therefore attribute the rapid rise of the mobility to disorder and hopping-distance effects.

Finally, we note that very similar parameters were used to account for all the experimental data, as illustrated by 5.1. Two relevant parameters are not included in

MODEL	F_z(meV/nm)	σ_0	α	X_C(meV $\cdot$ nm)	ρ_{carriers}(nm^{-3})	d_{crystal}(nm)	T(K)
μ_e	0.52	0.09	0.0121	827.26	0.002	0.44	300
μ_h	0.52	0.09	0.0121	827.26	0.002	0.44	300
σ_e	0.52	0.09	0.0854	827.26	0.002	0.44	300

Table 5.1: Parameters used for the simulations presented in 5.6. Crystal sizes were varied between 3-9nm throughout the simulation. Lattice dimensions were held at X=Y=5 and Z=200 sites.

the Table. HOMO and LUMO energies were directly taken from the calculations of Kang and Wise (5.3)[45], and the tunneling amplitudes were computed by the code of Brennan[11] as the half energy splittings in 5.2 divided by Planck's constant. Neither of these inputs contained any fitting or adjustment on our end. Finally, the simulations of 5.6b differ from 5.6a in the α parameter alone, which only serves as an overall scaling factor. The fact that nearly identical parameter sets are able to account for three sets of non-monotonic experimental data suggests that the hopping model incorporates the most significant energy terms and represents the most relevant physical processes.

5.5 Conclusion

A Monte Carlo model was developed to simulate electron and hole transport in ethane dithiol-capped PbSe nanocrystal films. The dependence of the calculated mobilities on the size of the nanocrystals is in excellent agreement with field effect measurements performed by Liu et al and by Kang et al.[54, 46] Simulations suggest that a sharp mobility increase for crystal sizes in the 3-5nm range can largely be attributed to two factors. (1) Carriers need fewer hops to cover a particular distance in films composed of larger nanocrystals. (2) Increasing crystal size decreases site energy disorder and

lowers hopping barriers. At larger crystals sizes (6-9nm), the mobilities exhibit a sloping downward trend. Two factors also drive this behavior. (1) The effective tunneling amplitudes decrease with increasing nanocrystal diameter. (2) Carriers are confined to fewer, larger nanocrystals, leading to more frequent carrier interactions. Transport paths encounter multiply occupied sites with increasing frequency, leading to increased carrier residence times.

The encouraging correlation between the simulations and the three experimental data sets supports that thermally assisted nearest neighbor tunneling is the dominant transport mechanism in the FET experiments of Liu et al and Kang et al.[54, 46]

Finally, our simulation's sensitivity to size disorder suggests that an emphasis on nanocrystal uniformity could dramatically improve the performance of nanocrystalline solar cells and transistors.

Chapter 6

Conclusion

In the first experiment presented in this thesis, we successfully fabricated conformal Cu_2S using CVD and PCVD deposition techniques. EXAFS and XPS measurements confirmed the Cu_2S stoichiometry in deposited materials, however sheet resistance and absorption measurements suggest the formation of a thin metallic layer of Cu-poor material at the substrate/film boundary. This is an obstacle to ETA device construction. In the second project, luminescent downshifting films were successfully utilized to improve the efficiencies of CdTe/CdS devices. Relative efficiency improvements of up to 8.5% were measured. Downshifting films proved stable under illumination when encapsulated in an oxygen and water free environment. Lastly, Monte Carlo simulations of carrier transport in nanocrystalline PbSe films were developed. Results are in excellent agreement with field effect conductivity/mobility measurements. Hopping distance, size disorder, inter-crystal tunneling, and carrier interactions appear to be the most important factors determining film mobilities and conductivities.

The three materials listed above represent some of the latest approaches to economical solar power. Cu_2S, LDS films, and PbSe are also at different stages of development and utility with relation to the solar industry. Though Cu_2S is a well established solar cell material, its stability is still not well understood. Controlling the material phase is still a hurdle to large scale device production. Though CVD provides a promising tool to ETA device fabrication, it is also not clear that it would be a cost effective technique for large scale device fabrication. CVD requires very low pressures, and this can be very expensive when done on a large scale. The Cu_2S stability concerns and the CVD cost challenges likely mean that commercial ETA Cu_2S devices are many years down the road.

Luminescent downshifting technologies, on the other hand, are already penetrating the photovoltaics industry. Solar greenhouses that employ downshifting films to concentrate sunlight are in the early stages of commercial trials. Utilizing downshifting films for spectrum modification in existing device structures is also a real possibility. CIGS solar cells suffer similar parasitic absorption problems to CdTe/CdS devices. They also require an encapsulation layer to protect the solar-converting materials from oxygen and water. With industry backing, downshifting films could be incorporated in commercial technologies within the next decade.

Devices constructed from nanocrystalline materials show tremendous potential, however they still quite young and unproven. Solution processability means that NC PbSe and similar materials could be produced at the industrial scale, however most materials are only being produced at the laboratory scale and are still quite expen-

sive. Carrier generation and transport in nanocrystalline materials are also not well understood. Though device efficiencies have been improving at an impressive rate, it is too early to tell if the nanomaterials will ever rival crystalline silicon's efficiency and affordability.

The work presented in this dissertation highlights some of the opportunities and challenges surrounding new solar technologies. Alternative materials and fabrication techniques open the door to cheap, efficient devices, but new materials must be defect-free and robust. We must also develop a basic understanding of these materials so that they can be used effectively.

According to a 2012 study, "grid-parity events will occur throughout the next decade in the majority of all market segments in the world"[12] The US will likely begin to achieve solar grid parity between 2016 and 2020.[12] In order facilitate these changes, solar must become more reliable. It must become cheaper, and the technology must convert electricity more efficiently. Lastly, new solar technologies must be accompanied by a restructuring of energy policies. Fossil fuel industries must be forced to consider the hidden costs of extraction and power generation. Globally, governments must cooperate to reduce CO_2 emissions rather than compete over existing reserves. With these developments we could witness the beginning of a clean energy revolution.

Bibliography

[1] U.S. Energy Information Administration. Electric power monthly March 2013, 2013.

[2] Ruona Agbroko. S.Africa imposes fracking moratorium in karoo. *Reuters*, April 2011.

[3] International Energy Agency. World energy outlook 2013. Reported by IEA 2013.

[4] U.S. Environmental Protection Agency. How does electricity affect the environment? http://www.epa.gov/cleanenergy/energy-and-you/affect/index.html. The U.S. Environmental Protection Agency's Clean Energy Programs are designed to improve the national foundation of information on clean energy by creating networks between the public and private sector, providing technical assistance, and offering recognition of environmental leaders that adopt clean energy practices.

[5] AM Aldhafiri, GJ Russell, and J Woods. Degradation in CDS-Cu2S photovoltaic cells. *Semiconductor Science and Technology*, 7(8):1052–1057, August 1992.

[6] J. M. An, A. Franceschetti, and A. Zunger. Electron and hole addition energies in pbse quantum dots. *Phys. Rev. B*, 76:045401, Jul 2007.

[7] A. D. Andreev, E. V. Kolobkova, and A. A. Lipovskii. Optical absorption in pbse spherical quantum dots embedded in glass matrix. *Journal of Applied Physics*, 88(2):750–757, 2000.

[8] Juan A. Anta, Jenny Nelson, and N. Quirke. Charge transport model for disordered materials: application to sensitized tio$_2$. *Phys. Rev. B*, 65:125324, Mar 2002.

[9] BP. BP statistical review of world energy June 2013., 2013.

[10] J.A. Bragagnolo, A.M. Barnett, J.E. Phillips, R.B. Hall, A. Rothwarf, and J.D. Meakin. The design and fabrication of thin-film CdS/Cu2S cells of 9.15-percent conversion efficiency. *Electron Devices, IEEE Transactions on*, 27(4):645–651, 1980.

[11] Kevin F. Brennan. A computer-aided approach to teaching band structure formation. *Education, IEEE Transactions on*, 35(1):60–68, 1992.

[12] Christian Breyer and Alexander Gerlach. Global overview on grid-parity. *Progress in Photovoltaics: Research and Applications*, page n/an/a, 2012.

[13] M. Burgelman and H.J. Pauwels. Theoretical advantages of pn+-type Cu2S-ZnO solar cell. *Electronics Letters*, 17(6):224–226, 1981.

[14] H. Bssler. Charge transport in disordered organic photoconductors a monte carlo simulation study. *physica status solidi (b)*, 175(1):15–56, 1993.

[15] J. Cardoso, O. Gomez-Daza, L. Ixtlilco, M. T. S. Nair, and P. K. Nair. Conductive copper sulfide thin films on polyimide foils for optical and optoelectronic applications. *Modern Physics Letters B*, 15(17/18/19):774, 2001.

[16] M. J. Cass, Alison B. Walker, D. Martinez, and L. M. Peter. Grain morphology and trapping effects on electron transport in dye-sensitized nanocrystalline solar cells. *The Journal of Physical Chemistry B*, 109(11):5100–5107, 2005.

[17] R. E. Chandler, A. J. Houtepen, J. Nelson, and D. Vanmaekelbergh. Electron transport in quantum dot solids: Monte carlo simulations of the effects of shell filling, coulomb repulsions, and site disorder. *Physical Review B*, 75(8):085325, February 2007.

[18] K. L. Chopra, P. D. Paulson, and V. Dutta. Thin-film solar cells: an overview. *Progress in Photovoltaics: Research and Applications*, 12(23):69–92, March 2004.

[19] K.L. Chopra and S.R. Das. *Thin Film Solar Cells*. Springer, 1 edition, July 1983.

[20] S. Couve, L. Gouskov, L. Szepessy, J. Vedel, and E. Castel. Resistivity and optical transmission of CuxS layers as a function of composition. *Thin Solid Films*, 15(2):223–231, February 1973.

[21] Richard J. Davies. Methane contamination of drinking water caused by hydraulic fracturing remains unproven. *Proceedings of the National Academy of Sciences*, 108(43):E871–E871, October 2011.

[22] Ibrahim Dincer. Renewable energy and sustainable development: a crucial review. *Renewable and Sustainable Energy Reviews*, 4(2):157 – 175, 2000.

[23] Hui Du, Chialing Chen, Rishikesh Krishnan, Todd D. Krauss, Jeffrey M. Harbold, Frank W. Wise, Malcolm G. Thomas, and John Silcox. Optical properties of colloidal pbse nanocrystals. *Nano Letters*, 2(11):1321–1324, 2002.

[24] Simon Elegant. Where the coal is stained with blood. *Time*, March 2007.

[25] Randy J. Ellingson, Matthew C. Beard, Justin C. Johnson, Pingrong Yu, Olga I. Micic, Arthur J. Nozik, Andrew Shabaev, and Alexander L. Efros. Highly efficient multiple exciton generation in colloidal pbse and pbs quantum dots. *Nano Letters*, 5(5):865–871, 2005.

[26] Saim Emin, Surya P. Singh, Liyuan Han, Norifusa Satoh, and Ashraful Islam. Colloidal quantum dot solar cells. *Solar Energy*, 85(6):1264 – 1282, 2011.

[27] K Ernst, A Belaidi, and R Konenkamp. Solar cell with extremely thin absorber on highly structured substrate. *SEMICONDUCTOR SCIENCE AND TECHNOLOGY*, 18(6):475–479, JUN 2003.

[28] Center for Responsive Politics. OpenSecrets.org: money in politics – see who's giving & who's getting. http://www.opensecrets.org/.

[29] Center for Responsive Politics. The terrorism index: A survey of the U.S. national security establishment on the war on terror. *Foreign Policy Magazine*, June 2006.

[30] S. David Freeman. *Winning Our Energy Independence: An Energy Insider Shows How.* Gibbs Smith, September 2007.

[31] David J. Griffiths. *Introduction to Electrodynamics.* Addison-Wesley, 4 edition, October 2012.

[32] Ivan Grozdanov and Metodija Najdoski. Optical and electrical properties of copper sulfide films of variable composition. *Journal of Solid State Chemistry*, 114(2):469–475, February 1995.

[33] Hartmut Haug and Stephan W. Koch. *Quantum Theory Of The Optical And Electronic Properties Of Semiconductors.* World Scientific Publishing Company, 5 edition, January 2009.

[34] Michael Hendryx and Melissa M. Ahern. Relations between health indicators and residential proximity to coal mining in west virginia. *American Journal of Public Health*, 98(4):669–671, April 2008.

[35] Jack Hollander. *The Energy-Environment Connection.* Island Press, August 1992.

[36] BC Hong and K Kawano. Organic dye-doped thin films for wavelength conversion and their effects on the photovoltaic characteristics of CdS/CdTe solar cell. *JAPANESE JOURNAL OF APPLIED PHYSICS*, 43(4A):1421–1426, 2004.

[37] Byung-Chul Hong and Katsuyasu Kawano. PL and PLE studies of KMgF3:Sm crystal and the effect of its wavelength conversion on CdS/CdTe solar cell. *Solar Energy Materials and Solar Cells*, 80(4):417–432, December 2003.

[38] H.J. Hovel, R.T. Hodgson, and J.M. Woodall. The effect of fluorescent wave-length shifting on solar cell spectral response. *Solar Energy Materials*, 2(1):19–29, September.

[39] John David Jackson. *Classical Electrodynamics Third Edition*. Wiley, 3 edition, August 1998.

[40] Robert B. Jackson, Stephen G. Osborn, Avner Vengosh, and Nathaniel R. Warner. Reply to davies: Hydraulic fracturing remains a possible mechanism for observed methane contamination of drinking water. *Proceedings of the National Academy of Sciences of the United States of America*, 108(43):E872–E872, October 2011.

[41] C. Jezewski, W. A Lanford, J. J Senkevich, D. Ye, T. M Lu, and C. Jin. Copper penetration into porous ultralow methyl silsesquioxane during selective CVD. *Chemical Vapor Deposition*, 9(6):305–307, December 2003.

[42] Johanna Johansson, Juhana Kostamo, Maarit Karppinen, and Lauri Niinist. Growth of conductive copper sulfide thin films by atomic layer deposition. *Journal of Materials Chemistry*, 12(4):1022–1026, March 2002.

[43] Jeffery Jones, Rita Devlin Marier, Randall Palmer, and Sofina Mirza-Reid. Quebec minister signals stricter ban on fracking. *Reuters*, September 2012.

[44] I Kaiser, K Ernst, Ch.-H Fischer, R Knenkamp, C Rost, I Sieber, and M.Ch Lux-Steiner. The eta-solar cell with cuins2: A photovoltaic cell concept using an ex-

tremely thin absorber (eta). *Solar Energy Materials and Solar Cells*, 67(14):89 – 96, 2001. ¡ce:title¿PVSEC 11 - {PART} III¡/ce:title¿.

[45] Inuk Kang and Frank W. Wise. Electronic structure and optical properties of pbs and pbse quantum dots. *J. Opt. Soc. Am. B*, 14(7):1632–1646, Jul 1997.

[46] Moon Sung Kang, Ayaskanta Sahu, David J. Norris, and C. Daniel Frisbie. Size- and temperature-dependent charge transport in pbse nanocrystal thin films. *Nano Letters*, 11(9):3887–3892, 2011.

[47] Ingrid Kelley. *Energy in America: A Tour of Our Fossil Fuel Culture and Beyond.* Vermont, December 2008.

[48] Efthymios Klampaftis, David Ross, Keith R. McIntosh, and Bryce S. Richards. Enhancing the performance of solar cells via luminescent down-shifting of the incident spectrum: A review. *Solar Energy Materials and Solar Cells*, 93(8):1182 – 1194, 2009.

[49] Victor I. Klimov. Detailed-balance power conversion limits of nanocrystal-quantum-dot solar cells in the presence of carrier multiplication. *Applied Physics Letters*, 89(12):123118, 2006.

[50] B. M Krasovitskii and B. M Bolotin. *Organic luminescent materials.* VCH, Weinheim; New York, NY, USA, 1988.

[51] Jihye Lee, One Choi, and Eunji Sim. Nonmonotonic size-dependent carrier mobility

in pbse nanocrystal arrays. *The Journal of Physical Chemistry Letters*, 3(6):714–719, 2012.

[52] Jin-Hong Lee, Kyung-Hee Ko, and Byung-Ok Park. Electrical and optical properties of ZnO transparent conducting films by the sol-gel method. *Journal of Crystal Growth*, 247(1-2):119–125, January 2003.

[53] Guangming Liu, T. Schulmeyer, J. Brtz, A. Klein, and W. Jaegermann. Interface properties and band alignment of Cu2S/CdS thin film solar cells. *Thin Solid Films*, 431-432:477–482, May 2003.

[54] Yao Liu, Markelle Gibbs, James Puthussery, Steven Gaik, Rachelle Ihly, Hugh W. Hillhouse, and Matt Law. Dependence of carrier mobility on nanocrystal size and ligand length in pbse nanocrystal solids. *Nano Letters*, 10(5):1960–1969, 2010.

[55] David J. C. MacKay. *Sustainable energy–without the hot air.* UIT, Cambridge, England, 2009.

[56] Otfried Madelung. *Semiconductors - Basic Data.* Springer, 2nd revised ed. edition, April 1996.

[57] R. A. Marsh, C. Groves, and N. C. Greenham. A microscopic model for the behavior of nanostructured organic photovoltaic devices. *Journal of Applied Physics*, 101(8):083509, 2007.

[58] Alex B. F. Martinson, Jeffrey W. Elam, and Michael J. Pellin. Atomic layer depo-

sition of cu[sub 2]S for future application in photovoltaics. *Applied Physics Letters*, 94(12):123107, 2009.

[59] Toshiro Maruyama and Ryota Kitamura. Transformations of the wavelength of the light incident upon CdS/CdTe solar cells. *Solar Energy Materials and Solar Cells*, 69(1):61–68, August 2001.

[60] Toshiro Maruyama and Ryota Kitamura. Transformations of the wavelength of the light incident upon solar cells. *Solar Energy Materials and Solar Cells*, 69(3):207–216, October 2001.

[61] Jason McLure. Vermont poised to be first state to outlaw fracking. *Reuters*, May 2012.

[62] Allen Miller and Elihu Abrahams. Impurity conduction at low concentrations. *Phys. Rev.*, 120:745–755, Nov 1960.

[63] Steve Mohr, Mikael Hk, Gavin Mudd, and Geoffrey Evans. Projection of long-term paths for australian coal production comparisons of four models. *International Journal of Coal Geology*, 86(4):329 – 341, 2011.

[64] B. J. Mulder. Optical properties of crystals of cuprous sulphides (chalcosite, djurleite, Cu1.9S, and digenite). *Physica Status Solidi (a)*, 13(1):79–88, September 1972.

[65] M T S Nair, L Guerrero, and P K Nair. Conversion of chemically deposited CuS

thin films to Cu1.8S and Cu1.96S by annealing. *SEMICONDUCTOR SCIENCE AND TECHNOLOGY*, 13(10):1164–1169, October 1998.

[66] M T S Nair and P K Nair. Chemical bath deposition of CuxS thin films and their prospective large area applications. *Semiconductor Science and Technology*, 4:191, 1989.

[67] I. Nakai, Y. Sugitani, K. Nagashima, and Y. Niwa. X-ray photoelectron spectroscopic study of copper minerals. *Journal of Inorganic and Nuclear Chemistry*, 40(5):789–791, 1978.

[68] Jenny Nelson. Continuous-time random-walk model of electron transport in nanocrystalline TiO_2 electrodes. *Physical Review B*, 59(23):15374–15380, June 1999.

[69] Jenny Nelson. *The Physics of Solar Cells*. Imperial College Press, 1 edition, September 2003.

[70] John A.T. Norman, Melanie Perez, Stefan E. Schulz, and Thomas Waechtler. New precursors for CVD copper metallization. *Microelectronic Engineering*, 85(10):2159–2163, October 2008.

[71] U.S. Bureau of Labor Statistics. Census of fatal occupational injuries (CFOI) - current and revised data. Reported by BLS 2011.

[72] U.S. Bureau of Labor Statistics. Labor force statistics (current population survey - cps). Reported by BLS 2013.

[73] Stephen G. Osborn, Avner Vengosh, Nathaniel R. Warner, and Robert B. Jackson. Methane contamination of drinking water accompanying gas-well drilling and hydraulic fracturing. *Proceedings of the National Academy of Sciences*, 108(20):8172–8176, May 2011.

[74] Tara Patel. France to keep shale ban until fracking alternative emerges. *Business-Week: undefined*, August 2012.

[75] J. J. H. Pijpers, R. Ulbricht, K. J. Tielrooij, A. Osherov, Y. Golan, C. Delerue, G. Allan, and M. Bonn. Assessment of carrier-multiplication efficiency in bulk PbSe and PbS. *Nat Phys*, 5(11):811–814, November 2009.

[76] L.G. Rainhart and W.P. Schimmel Jr. Effect of outdoor aging on acrylic sheet. *Solar Energy*, 17(4):259 – 264, 1975.

[77] L. Reijnen, B. Meester, A. Goossens, and J. Schoonman. Nanoporous TiO2/Cu1.8S heterojunctions for solar energy conversion. *Materials Science and Engineering: C*, 19(1-2):311–314, January 2002.

[78] L. Reijnen, B. Meester, A. Goossens, and J. Schoonman. Atomic layer deposition of CuxS for solar energy conversion. *Chemical Vapor Deposition*, 9(1):15–20, January 2003.

[79] Liesbeth Reijnen, Ben Meester, Frits de Lange, Joop Schoonman, and Albert Goossens. Comparison of CuxS films grown by atomic layer deposition and chemical vapor deposition. *Chemistry of Materials*, 17(10):2724–2728, May 2005.

[80] B.S. Richard and A. Shalav. The role of polymers in the luminescence conversion of sunlight for enhanced solar cell performance. *Synthetic Metals*, 154(13):61 – 64, 2005. ¡ce:title¿Proceedings of the International Conference on Science and Technology of Synthetic Metals¡/ce:title¿ ¡ce:subtitle¿Part III¡/ce:subtitle¿.

[81] B.S. Richards and K.R. McIntosh. Overcoming the poor short wavelength spectral response of CdS/CdTe photovoltaic modules via luminescence down-shifting: ray-tracing simulations. *Progress in Photovoltaics: Research and Applications*, 15(1):27–34, January 2007.

[82] Paul Roberts. *The End of Oil: On the Edge of a Perilous New World.* Mariner Books, April 2005.

[83] Sumner SA and Layde PM. Expansion of renewable energy industries and implications for occupational health. *JAMA: The Journal of the American Medical Association*, 302(7):787–789, 2009.

[84] R. D. Schaller and V. I. Klimov. High efficiency carrier multiplication in pbse nanocrystals: Implications for solar energy conversion. *Phys. Rev. Lett.*, 92:186601, May 2004.

[85] Harvey Scher and Elliott W. Montroll. Anomalous transit-time dispersion in amorphous solids. *Phys. Rev. B*, 12:2455–2477, Sep 1975.

[86] Octavi E. Semonin, Justin C. Johnson, Joseph M. Luther, Aaron G. Midgett, Arthur J. Nozik, and Matthew C. Beard. Absolute photoluminescence quantum

yields of ir-26 dye, pbs, and pbse quantum dots. *The Journal of Physical Chemistry Letters*, 1(16):2445–2450, 2010.

[87] Dmitri V. Talapin and Christopher B. Murray. Pbse nanocrystal solids for n- and p-channel thin film field-effect transistors. *Science*, 310(5745):86–89, 2005.

[88] William A. Tisdale, Kenrick J. Williams, Brooke A. Timp, David J. Norris, Eray S. Aydil, and X.-Y. Zhu. Hot-electron transfer from semiconductor nanocrystals. *Science*, 328(5985):1543–1547, 2010.

[89] Ian Urbina. South african farmers see threat from fracking. *The New York Times*, December 2011.

[90] Daniel Vanmaekelbergh and Peter Liljeroth. Electron-conducting quantum dot solids: novel materials based on colloidal semiconductor nanocrystals. *Chem. Soc. Rev.*, 34:299–312, 2005.

[91] Ralf Vogel, Klaus Pohl, and Horst Weller. Sensitization of highly porous, polycrystalline tio2 electrodes by quantum sized cds. *Chemical Physics Letters*, 174(34):241 – 246, 1990.

[92] Matthew L. Wald. Fossil fuels hidden cost is in billions, study says. *The New York Times*, October 2009.

[93] Peter K. Watkins, Alison B. Walker, and Geraldine L. B. Verschoor. Dynamical monte carlo modelling of organic solar cells: the dependence of internal quantum efficiency on morphology. *Nano Letters*, 5(9):1814–1818, 2005. PMID: 16159229.

[94] Frank W. Wise. Lead salt quantum dots: the limit of strong quantum confinement. *Accounts of Chemical Research*, 33(11):773–780, 2000. PMID: 11087314.

[95] Richard Wolfson. *Energy, environment, and climate.* W.W. Norton & Company, New York, 2012.

[96] X. Wu, R. G. Dhere, D. S. Albin, T. A. Gessert, C. Dehart, J. C. Keane, A. Duda, T. J. Coutts, S. Asher, D. H. Levi, et al. High-efficiency CTO/ZTO/CdS/CdTe polycrystalline thin-film solar cells. In *NREL/NCPV Program Review Meeting*, page 1417, 2001.

[97] Hongping Yan, Sufal Swaraj, Cheng Wang, Inchan Hwang, Neil C. Greenham, Chris Groves, Harald Ade, and Christopher R. McNeill. Influence of annealing and interfacial roughness on the performance of bilayer donor/acceptor polymer photovoltaic devices. *Advanced Functional Materials*, 20(24):4329–4337, 2010.

[98] Fan Yang and Stephen R. Forrest. Photocurrent generation in nanostructured organic solar cells. *ACS Nano*, 2(5):1022–1032, 2008.

[99] Bart Van Zeghbroeck. *Principles of Semiconductor Devices and Heterojunctions.* Prentice Hall PTR, November 2007.